

THESIS FOR THE DEGREE OF DOCTOR OF PHILOSOPHY

Nano-particulate Silica Hydrogels Imaged in 2D and 3D using TEM

Effects of local pore structure on mass transport and applications in
aggregation dynamics

CHARLOTTE HAMNGREN BLOMQVIST



Department of Physics
CHALMERS UNIVERSITY OF TECHNOLOGY
Gothenburg, Sweden 2016

Nano-particulate Silica Hydrogels Imaged in 2D and 3D using TEM: Effects of local pore structure on mass transport and applications in aggregation dynamics
Charlotte Hamngren Blomqvist

© Charlotte Hamngren Blomqvist, 2016.

ISBN 978-91-7597-519-1

Doktorsavhandlingar vid Chalmers tekniska högskola
Ny serie Nr 4200
ISSN 0346-718X

Department of Physics
Chalmers University of Technology, SE-412 96 Göteborg
Tel: +46 (0)31-7721000
<http://www.chalmers.se/ap/EN>

Cover image:

Top: A cut-out from an electron tomogram of a particulate silica hydrogel, displaying the 3D structure of the nanoparticles of $\varnothing = 22$ nm in detail. **Left:** A scanning transmission electron micrograph of large field-of-view, showing the 2D structure of the particulate silica hydrogel. **Right:** Lattice-Boltzmann flow simulations performed *in situ* and in 3D through Gel 2. Image courtesy of Tobias Gebäck.

Printed by Chalmers Reproservice
Göteborg, Sweden, 2016

Nano-particulate Silica Hydrogels Imaged in 2D and 3D using TEM: Effects of local pore structure on mass transport and applications in aggregation dynamics

Charlotte Hamngren Blomqvist

Department of Physics Chalmers University of Technology

Abstract

Porous materials are frequently used in everyday applications including food science, pharmaceuticals, fuel cell membranes, batteries and solar cells. A key aspect in these porous materials is how their micro- and nano-structure affect the internal transport of for example water, particles or charges. The transport is a three-dimensional process. Therefore, structure information in three dimensions is especially important when analysing and further improving as well as developing new types of porous materials. In this thesis, I used Electron Tomography (ET) to directly reveal and quantify the three-dimensional structure of one type of soft porous material on the nano-scale.

Three different nanoscale Particulate Silica Hydrogel (PSH) samples were synthesised and examined regarding the relationship of material nanostructure to both mass transport and particle aggregation dynamics. The PSH samples had equal percentage of silica, but had particle sizes ranging from 3.6 nm to 22 nm, and different aggregation parameters which rendered structural differences between the samples.

The samples were imaged in two dimensions using Scanning Transmission Electron Microscopy (STEM) and in three dimensions using ET. The two-dimensional STEM micrographs were examined using stereological and geometrical image analysis. The water transport properties of the PSHs were studied by direct measurements, Nuclear Magnetic Resonance (NMR) diffusometry and by *in situ* Lattice-Boltzmann Modelling (LBM).

In both two and three dimensions, we determined the local structure of the different PSHs. We quantified the characteristics of the PSHs concerning primary particle shape in two dimensions and geometrical pore size distribution in two and three dimensions. Here, we highlight both the nanostructure of the *particle* network and the connectivity of the *pore* network, seeing indications that the finer two gels had more narrow pore throats than the coarser gel. The pore size distribution had a minimal impact on water permeability below a pore size of 120 nm. Despite the almost identical flow properties of the two finer gels, they showed large differences concerning the accessible pore volume fraction in relation to their mean pore size. The LBM simulations showed higher values than the experiments for the permeability of the gels. Hence, a comparative study of simulated PSH sections was performed, from which it was clear that the simulation templates needed to be thicker in order to provide values more coherent to the experimental data.

We have proposed and demonstrated an approach for estimating the three dimensional structure from two-dimensional STEM micrographs, using the intensity profile as a structure parameter in the third dimension. From the 2D data, we concluded that the Reaction Limited Cluster Aggregation process (RLCA) explains the structure of the particle network in the hydrogels better than the Diffusion Limited Cluster Aggregation process (DLCA) does. However, there is not a perfect match. Our preliminary results show that the acquired three-dimensional data agrees significantly better to the RLCA model compared to the two-dimensional data.

This thesis addresses the liquid flow properties of PSHs and the relation between liquid flow and nanoscale structure, including the interconnectivity of the pore network. Thus, contributing to the field of mass transport in nanoscale porous materials. We also predict ET to be applied more frequently in the field of particulate hydrogels, including e.g. controlled release, battery and biomedical applications.

Keywords: electron tomography, silica gel, silica nanoparticle gel, colloidal silica gel, accessible volume fraction, interconnectivity, nanostructure, 3D structure, nanoporous, mass transport.

To my beloved family

LIST OF PUBLICATIONS

This thesis is based on the work contained in the following scientific papers, referred to by Roman numerals in the text:

I Estimation of Mass Thickness Response of Embedded Aggregated Silica Nanospheres from High Angle Annular Dark-Field Scanning Transmission Electron Micrographs

M. Nordin, C. Abrahamsson, C. Hamngren Blomqvist, H. Häbel, M. Röding, E. Olsson, M. Nydén, and M. Rudemo.
Journal of Microscopy, **253**, (2), 166-170, (2014).

II Pore Size Effects on Convective Flow and Diffusion Through Nanoporous Silica Gels

C. Hamngren Blomqvist, C. Abrahamsson, T. Gebäck, A. Altskär, A.-M. Hermansson, M. Nydén, S. Gustafsson, N. Lorén, and E. Olsson.
Colloids and Surfaces A: Physicochemical and Engineering Aspects, **484**, 288-296, (2015)

III From Static Micrographs to Particle Aggregation Dynamics in Three Dimensions

H. Häbel, A. Särkkä, M. Rudemo, C. Hamngren Blomqvist, E. Olsson, C. Abrahamsson, and M. Nordin.
Journal of Microscopy, **262**, (1), 102-111, (2016).

IV Interconnectivity Imaged in Three Dimensions: Nano-particulate Silica-Hydrogel Structure Revealed Using Electron Tomography

C. Hamngren Blomqvist, T. Gebäck, A. Altskär, A.-M. Hermansson, S. Gustafsson, N. Lorén, and E. Olsson
In manuscript.

V Three-dimensional Analysis of Nanoscale Pore-morphology and Simulated Mass Transport in Particulate Silica Hydrogels

C. Hamngren Blomqvist, T. Gebäck, H. Häbel, A. Altskär, A.-M. Hermansson, S. Gustafsson, N. Lorén, A. Särkkä, and E. Olsson
In manuscript.

In addition to the papers listed above, I have contributed to the following papers, which are not included in the thesis:

Colloidal Particle Aggregation in Three Dimensions

H. Häbel, C. Hamngren Blomqvist, A. Särkkä, M. Rudemo, E. Olsson, and M. Nordin.
In manuscript.

A Single-Cell Study of a Highly Effective Hog1 Inhibitor for *in Situ* Yeast Cell Manipulation

C. Hamngren Blomqvist, P. Dinér, M. Grøtli, M. Goksör, and C. B. Adiels.
Micromachines, **5**, 81-96, (2014).

Design and Evaluation of a Microfluidic System for Inhibition Studies of Yeast Cell Signaling

C. Hamngren, P. Dinér, M. Grøtli, M. Goksör, and C. B. Adiels.
Optical Trapping and Optical Micromanipulation IX, edited by Kishan Dholakia, Gabriel C. Spalding, Proc. of SPIE Vol. 8458, (2012). doi: 10.1117/12.929728

CONTRIBUTION REPORT

Paper I. I performed the thin sectioning of the sample, the HAADF-STEM imaging and the HAADF-detector inner-radius measurements. I wrote the Material and methods parts on plastic embedding and thin sectioning.

Paper II. I prepared and embedded two of the three gels. I performed the thin sectioning for electron microscopy and all 2D imaging. I performed the ET, including image alignment, reconstruction and visualisation. I co-wrote the code for the stereological image analysis and micrograph binarisation. I performed the stereological image analysis. I performed the macroscopic visual inspection, and the size and shape analysis of the particles constituting two of the samples. I wrote the draft of the paper, compiled the input from the co-authors and coordinated the work on finalising the paper.

Paper III. I performed the thin sectioning and the STEM imaging of the gel sample. I advised on the writing of the Material and methods section.

Paper IV. I prepared and embedded two of the three gels. I performed the thin sectioning for electron microscopy and all 2D imaging and image processing. I performed the ET, including image alignment, reconstruction and visualisation. I wrote the draft of the paper, compiled the input from the co-authors and coordinated the work on finalising the paper.

Paper V. I prepared and embedded two of the three gels. I performed the thin sectioning for electron microscopy and the ET, including image alignment, reconstruction and visualisation. I wrote the draft of the paper, compiled the input from the co-authors and coordinated the work on finalising the paper.

PREFACE

The research presented in my thesis was carried out at Chalmers University of Technology (Göteborg, Sweden), in the Eva Olsson group at the Department of Physics.¹ The main part of the thesis work was performed from February 2011 to April 2015; and from July 2016 to December 2016. The project was a part of the VINN EXCELLENCE centre Supramolecular Biomaterials (SuMo), and the work was conducted under supervision by Prof. Eva Olsson and Prof. Anne-Marie Hermansson, assistant supervisors Dr. Stefan Gustafsson and Adj. Prof. Niklas Lorén, and mentor Annika Altskär.

Göteborg, 15th December 2016
Charlotte Hamngren Blomqvist

LIST OF ABBREVIATIONS

2D	Two-dimensional or two dimensions
3D	Three-dimensional or three dimensions
AMD	Arithmetic mean diameter
CCD	Charge-coupled device
DLCA	Diffusion limited cluster aggregation
ET	Electron tomography
FEG	Field emission gun
HAADF	High-angular annular dark field
ISA	Intrinsic surface area
LBM	Lattice-Boltzmann model/ling
MW	Missing wedge
NMR	Nuclear magnetic resonance
PSD	Pore size distribution
PSH	Particulate silica hydrogel
RLCA	Reaction limited cluster aggregation
SIRT	Simultaneous iterative reconstruction technique
STEM	Scanning transmission electron microscope/y
TEM	Transmission electron microscope/y
VWMV	Volume-weighted mean volume
WBP	Weighted back projection

¹The Department of Physics was formed in 2016 from the merging of the former Department of Applied Physics and the Department of Fundamental Physics.

Contents

1	Introduction	1
1.1	Scope of work	3
2	Methodology	5
2.1	Particulate silica hydrogels (PSH)	5
2.2	Aggregation dynamics	6
2.3	Transmission electron microscopy: TEM and STEM	6
2.4	Electron tomography (ET)	7
2.5	Mass transport	9
3	Experimental	15
3.1	From colloid to electron microscopy sample	15
3.2	Transmission electron microscopy studies	20
3.3	Mass transport measurements	21
4	Data analysis and computer simulations	23
4.1	Image analysis	23
4.2	Principles of Electron Tomography (ET) post processing	27
4.3	Interconnectivity and accessible pore volume fraction analysis	28
4.4	Mass transport analysis	29
5	Summary of results and discussion	31
5.1	PSH structure in 2D and 3D	31
5.2	Structure vs. fluid transport properties in particulate silica hydrogels	43
5.3	Aggregation dynamics during gelation of particular silica hydrogels	46
5.4	Experimental considerations for ET on PSHs	47
6	Summary of included papers	49
6.1	Paper I	50
6.2	Paper II	50
6.3	Paper III	51
6.4	Paper IV	51
6.5	Paper V	53
7	Summary of work	55
7.1	Conclusions	55
7.2	Outlook	56
	References	61
	Papers I–V	

Chapter 1

Introduction

Porous materials are frequently applied in everyday applications including food science [1], pharmaceuticals[2], catalysts[3, 4], fuel cell membranes[5], batteries[6–8] and solar cells[9, 10], as well as being subject to fundamental research[11–13]. Soft porous materials constitute an important category of porous materials, which can be defined as ”[including but] not limited to: gels, polymers, colloids, vesicles, emulsions, films, surfactants, micelles, suspensions, liquid crystals, biological macromolecules, membranes, bio-composites and biomimetic materials”[14].

The size and morphology of the pores in a porous material have a large impact on its intrinsic transport properties concerning e.g. fluids, molecules, charges or cells. This transport is commonly denoted as *mass transport*[15], and determines the material performance in applications as diverse as controlled release[2] and battery science[6, 7]. Mass transport in general is strongly influenced by material structure, ranging from the molecular scale to the macroscopic scale. Influencing features are for example the porosity, the distribution of open pore space, pore throats or pore connectivity[1, 2, 16–22]. When the applied pressure is kept constant, convective flow is dominating over diffusion as the primary mass transport mechanism[1, 15, 23, 24] for pore sizes well above 200 nm. As the pore radius then decreases, the importance of diffusion is expected to increase rapidly due to smaller pore radiuses give rise to larger pressure drops, which is described by the Hagen-Poiseuille relationship[25],

$$Q = \frac{\pi R^4}{8L\eta} p. \quad (1.1)$$

Here, the pores are assumed straight, and the flow is steady and laminar. The flow rate is denoted Q , the pipe radius R , and the pipe length L . This transition region between diffusion and convective flow is not yet well understood in nano-structured materials. It is therefore of utmost importance to study the correlation between structure and transport properties in this regime.

Electron microscopy studies have confirmed that materials with pore sizes in the 200 nm-to-2 μm range are more predisposed to lose moisture, compared to materials structured on an even smaller scale[15, 23, 24]. Also, mass transport studies on materials with pores as small as 100 nm has recently been performed[11, 26] using microscopic techniques to reveal the material structure. The mentioned microscopy studies were all carried out in two dimensions, using projected images of a thin sample. However, in order to describe how a medium travels through a porous-material structure, information from only 2D images is generally not enough[27]. Instead, three-dimensional descriptions of the material structure is needed. This necessity of three-dimensional imaging was confirmed in a diffusion study within a heterogeneous material, using two-dimensional micrographs[28]. The mentioned study show that two-dimensional microscopy underestimate the pore space accessible for water-molecule diffusion and the study suggests that water diffusion is influenced by the irregular shapes of the pores and the narrow pore throats between them. These calculations were made in two dimensions while mass transport in the studied material was three-dimensional. Hence, the effect of the connectivity in three dimensions was underestimated for

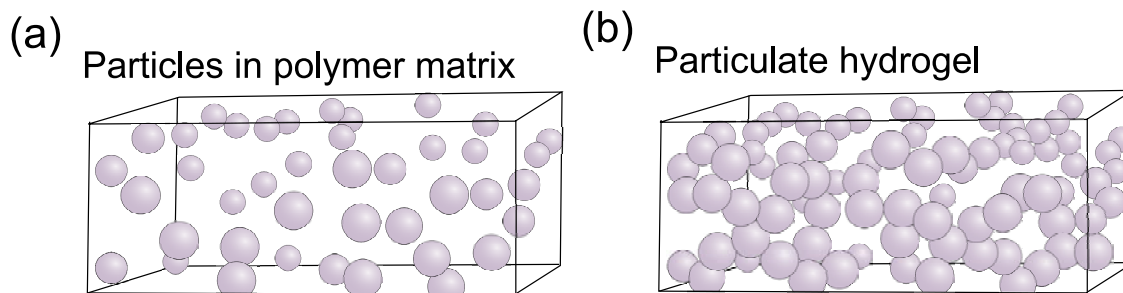


Figure 1.1: Schematic illustrations of the difference between (a) particles dispersed in a polymer matrix and (b) particulate hydrogels. The spheres represent the particles, and the surrounding area in the box represents the polymer matrix in (a) and the water phase of the hydrogel in (b). A particulate gel is defined by its continuous particle network as visible in (b).

larger pores.

Particulate silica hydrogels[29, 30] are highly relevant and useful systems for the study of e.g. mass transport and aggregation dynamics, since their structure is tuneable by changing for example the particle size and morphology, pH or ionic strength. Particulate hydrogels are composed of nanoparticles which bind to each other, forming a continuous 3D network on the macroscopic scale. The formation of the network is often described by spatial statistics in the field of aggregation dynamics. When the subunit-network spans the entire available volume, the gel point is reached and the material properties changes abruptly[31]. Silica provides a distinctive contrast in the electron microscope, without the need for additional staining[30]. From these perspectives particulate silica hydrogels are well suited for electron microscopy studies and material characterisation, focusing on either mass transport or particle aggregation dynamics.

Porous materials with pore sizes in the range 2-50 nm, are traditionally studied using various indirect methods[32–40], e.g. liquid intrusion or adsorption techniques, calorimetric methods or X-ray scattering techniques, providing mean values and distribution curves representing the whole volume of the studied sample. These techniques are often unsuitable, since they i) often require a dry sample and ii) the interpretation of the data assume a certain shape of the pores[41]. It is very common that the pore volume of a porous material is constituted from the space that is left in-between the network structure of the material, leaving the pore shapes highly irregular[32]. (This is the case for particulate silica hydrogels.) Any pre-formed assumption of a certain pore shape might therefore be misleading. Also, these indirect methods does not provide any local information about the structure.

In the beginning of my thesis work in 2011, Electron Tomography (ET) had been used within the physical sciences for only ten years[42], but porous materials with 1-5 nm pores had already been studied in three dimensions[43]. In the mentioned study, ET is presented as a unique measurement technique for accurate predictions of mechanical properties of nanoscale materials[43]. Nevertheless, the technique had not yet been used for studying mass transport within porous materials, nor had it been used for imaging any particulate hydrogel structures. There are now plenty of ET studies of single complex objects, such as nanoparticles[44] or nanoparticle aggregates or graphene dispersed in a polymer matrix[45–49]. The conceptual difference between 'particles dispersed in a polymer matrix', and a 'particulate hydrogel' network is shown in figure 1.1.

The analysis and handling of a hydrogel include many challenges since the gel contains water and is therefore sensitive to e.g. heat, radiation and mechanical strain or stress. The low pressure within a conventional electron-microscope-specimen chamber would cause evaporation of the water within the structure, possibly destroying the sample. Careful sample preparation was therefore crucial.

1.1 Scope of work

Even though flow and diffusion are three-dimensional processes, information concerning how the third spatial dimension of the structure affects flow and diffusion on the nanoscale is often not considered or only presented in the form of average values of statistics. The average values do not provide any information about the local structure. Also, there is a value in itself to actually see the structure of the material since it is relevant to both the material properties and to the formation of the material during fabrication. The local structure provides a better understanding of the consequences of pore connectivity and morphology than the indirect methods.

In this thesis work, I have focused on imaging and analysis of nanoscale Particulate Silica Hydrogels (PSH)s in 2D and 3D. The pore network structure and particle network structure have been studied in relation to mass transport properties and aggregation dynamics. For material analysis, I have used Transmission Electron Microscopy (TEM), Scanning Transmission Electron Microscopy (STEM) and ET. Image analysis, spatial statistics and mass transport measurements, have also been implemented in the study.

The 3D characterisation of the material structure provided an understanding of pore connectivity in the gels and also how the average pore size depended on the three-dimensional structure.

The three-dimensional reconstructions of the PSHs enabled Lattice-Boltzmann Modelling (LBM) mass transport simulations through the reconstructed tomograms of the gels, meaning that the simulations of flow and diffusion now can be performed in a three-dimensional replica of an *actual* material on the nanoscale. The reconstructions also enabled a digital replica of the actual gel to be used for comparison with the simulated gel structures, an important step of the evaluation process of the aggregation dynamics modelling.

The following research questions are addressed in this thesis:

- How can the local three-dimensional nanoscale structure and interconnectivity of particulate silica hydrogels be imaged in 3D?
 - Which possibilities are provided by using ET for structure determination?
 - Which limitations does ET suffer from when applied for slab samples of particulate silica hydrogels?
- When is 3D information necessary and when is 2D information sufficient as the following questioned are addressed?
 - How is the liquid transport within particulate silica hydrogels affected by the intrinsic pore structure?
 - Which aggregation dynamics model explains the formation of the PSH structure most accurately?
- How can the information of structure aggregation dynamics be deduced from two-dimensional STEM images?

Chapter 2

Methodology

2.1 Particulate silica hydrogels (PSH)

A common definition of a gel is a material composed of microscopic subunits (e.g. nanoparticles or polymer subunits) which bind to each other, forming a continuous 3D network on the macroscopic scale. When the subunit-network spans the entire available volume, the gel point is reached. Gel definitions differ between chemical and physical gels: chemical gels have covalently linked subunits, while physical gels are held together by physical interactions[31]. Gels are structurally disordered, and can display both solid and liquid-like properties. They can also contain large proportions of liquid[31]. A central subcategory of gels are particulate hydrogels (also called sol-gel materials[50] or colloidal gels). The terms particulate and colloidal are used interchangeably in this thesis. The particulate hydrogels are two-phase materials consisting of one continuous network of particles surrounded by water.

Amorphous silicon dioxide (SiO_2), also known as silica, is the most common compound of the Earth's crust[51]. PSH are chemical gels, which are essentially colloidal suspensions of nanoparticles (a *sol*) that have undergone a process of gelation. During gelation, the silica particles agglomerate into a continuous network that spans the available volume[52]. Within the amorphous silica aggregates, no boundaries can be detected *i.e.* the aggregate is the primary particle[45]. This observations correlate with my own experience of the material.

Aggregation of silica nanoparticles occurs spontaneously if the particles are uncharged. Hence, the silica sols always contains charged particles. The decharging of the particle surfaces can be initiated by changes in pH, ionic strength or both, which initialises the gelation process. The formation of the silica network starts with the formation of reversible siloxane bonds (Si-O-Si) between nanoparticles in contact. After this initial bonding, there will be an almost infinitely small negative radius of curvature between the particles. At this location, the solubility of silica is zero. Hence, silica residue from the solution initiates the neck-formation at the binding sites, making the adjacent particles merge together seamlessly and irreversibly as covalent bonds are formed[51].

PSH are capable of containing very large fractions of water, and can for example be used together with a gelling agent for ground consolidation of building sites[53, 54], or as a gelled electrolyte in Valve-Regulated Lead-Acid (VRLA) batteries[6, 7]. Today, particulate (or fumed) silica hydrogels in different configurations are increasingly studied[8, 55, 56], and used in for example battery science[6, 7], ground pollution prevention[54], controlled release[57, 58] and cell entrapment[59].

The mechanical and rheological properties of forming PSH (e.g. gelation time, gel strength and elastic modulus) have been thoroughly investigated as a function of ionic strength and solid volume fraction[51, 55, 56, 60]. However, the focus has been on the aggregation process during gelation, as a function of ionic strength and silica concentration, rather than the actual structure of the finished gel.

The first TEM images of a silica gel were presented on the third international conference of electron microscopy in London, 1954[30]. ET has been used for imaging dispersed silica aggregates[45], but has not earlier been used for imaging a particulate gel network.

Surface titration studies[61] previously performed¹ on the colloidal suspensions provided information about the nominal sizes for the silica spheres in the different sols[62]. The diameters were 22 ± 5 nm[11], 5.0 nm, and 3.6 nm, respectively[62].

2.2 Aggregation dynamics

Three-dimensional structures of particulate gels are built up as a function of different (unknown) probabilities for aggregation. The probability of aggregation between two particles or particle clusters that meet by means of Brownian motion is anywhere between 0 and 1. If the probability of cluster aggregation is 1, the only factor limiting the aggregation is the diffusion of the fluid surrounding the clusters.² Hence, this aggregation dynamics model is called Diffusion Limited Cluster Aggregation (DLCA). The cluster aggregation process can also be limited by the probability of the meeting particles or clusters reacting chemically with each other. The process is then referred to as Reaction Limited Cluster Aggregation (RLCA). The smaller the probability of cluster aggregation, the more prominent is the RLCA aspect of the aggregation dynamics. Different aggregation probabilities can be evaluated from simulated structures. It is consequently possible to determine which aggregation dynamics model is best suited for a specific particulate material, by comparison with an experimentally attained structure.

2.3 Transmission electron microscopy: TEM and STEM

In traditional visible light microscopes, photons in the form of visible light are used for creating images of microscopic objects. The resolution of an image is often defined as the minimum distance between two points that are still perceived as two points instead of one. A common estimation of the possible resolution (δ) in a microscope is the Rayleigh criterion,

$$\delta \approx \frac{1.22\lambda}{\beta}, \quad (2.1)$$

where λ denotes the wavelength of the photons, and the β denotes the semi collection-angle of the magnifying lens. This criterion sets the maximum possible resolution for a visible light microscope to approximately 300 nm[63]. One way to push the resolution even further is by using electrons with shorter wavelengths instead of photons. Electron microscopy is one of few techniques that can provide both spatial resolution on the sub Ångström scale and chemical information with high spatial resolution, i.e. on the sub nanometre scale.

Transmission electron microscopes were used for acquiring bright field TEM and High Angle Annular Dark-Field (HAADF) STEM (HAADF-STEM) micrographs of the sectioned samples. In the TEM, an image is formed by magnetic lenses, and can be displayed on a fluorescent screen or with a Charge-Coupled Device (CCD) camera, after the electron beam has interacted with the specimen.

The dominating contrast mechanism for amorphous materials (as both the silica gel and the embedding material is) is the mass thickness contrast. It originates from the difference in the degree of electron scattering by heavier and lighter elements. Heavier elements will scatter a higher proportion of electrons to higher angles compared to lighter elements. In the TEM, an objective aperture can be used to select different portions of the scattered electrons, enhancing the contrast of the image. For STEM imaging, an annular HAADF detector is placed in one of the focal planes collecting electrons scattered at higher angles, while the direct beam or less scattered

¹By the provider of the colloidal suspensions, AkzoNobel PPC AB

²Diffusion of the fluid controls the rate of the Brownian motion of the particle clusters.

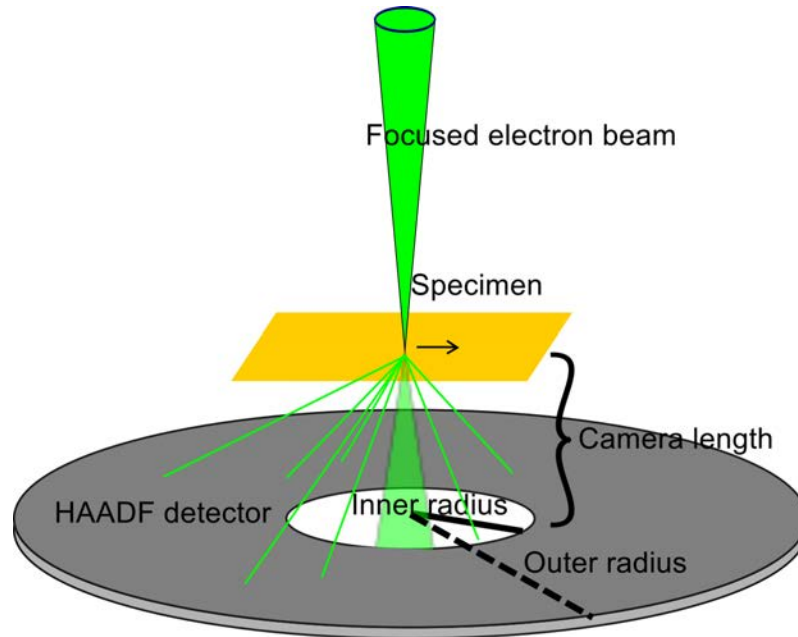


Figure 2.1: A schematic image of the principle of HAADF-STEM imaging. A focused electron beam is scanned over a part of the specimen. The thin green lines represent scattered electrons. Electrons scattered to high angles by the sample will be detected by the HAADF detector. The number of detected electrons for a specific position of the beam will determine the intensity value for the corresponding pixel in the acquired image. The camera length is the virtual distance between the specimen and the detector.

electrons will not be recorded, see figure 2.1. For the silica gel specimens (which have an even thickness), the silica particles will appear darker compared to the embedding plastic in TEM mode, and lighter than the embedding plastic in HAADF-STEM mode[63].

A TEM and STEM specimen needs to be thin in order for the beam to be able to penetrate the whole thickness of it. The image will be a 2D projection of the 3D structure present within the specimen. A typical specimen thickness for TEM is 100 nm or thinner.

2.4 Electron tomography (ET)

Conventional transmission electron microscopy commonly produce a projected image of the specimen. This means that the micrograph shows a representation of the sample which is non-unique (i.e. several particle configurations could theoretically give rise to identical projected images), and connectivity and spatial distribution in the depth direction are essentially missing.

Three-dimensional imaging techniques on the sub-micrometer length scale can be divided into three large subcategories[64]: focused ion beam scanning electron microscope (FIB-SEM) tomography (a *slice-and-view* technique), atom probe tomography (APT) and transmission electron microscope tomography, which can also be performed in scanning mode, using an annular detector. A primary difference between FIB-SEM, APT and ET is the length scale of the collected data:FIB-SEM is suitable for retrieving information on the micrometer scale, and APT can provide information with atomic resolution[64]. In the intermediate regime, ET is a powerful technique for determining the 3D structure on the nanometer scale.

The first implementation of ET (using TEM) was within the biological sciences[65]. Achievements in image-acquisition automation[66], lead to the application of ET within material science and

catalysis in early 21st century, using STEM[42, 67].

In order for an imaging technique to be suitable for tomographic reconstruction, the projection requirement must be fulfilled, meaning in principle that the tilted projections need to have a monotonic intensity relationship[68]. An example of a technique that fulfills this requirement of monotony is the STEM imaging, where more material in the direction of the beam will correspond to a higher detected intensity value in the image. STEM is now the most recommended technique for ET in the physical sciences[69].

ET is based on an image series of the specimen collected from different angles, either by imaging the same specimen while tilting the sample holder, or by using one or several images of many identical objects, with random orientation[70]. The latter approach is applicable when imaging several identical biological specimens, but not when working with irregular porous structures. For unique samples, a tilting approach is necessary in order to resolve the nanoscale spatial structure.

Tilting can be performed in different ways, e.g. single axis, or dual axis tilting as well as conical tilting or full rotation tilting. In single axis tilting, the specimen is tilted between two maximum tilt angles, e.g. from $+75^\circ$ to -75° [65], and the resulting collection of images is known as a "tilt series". The tilting can have either the same increment angle between each exposure (linear), or it can follow a so called Saxton scheme where more images are acquired at higher tilt angles, and less images are collected at lower tilt angles, in a continuous fashion. The Saxton scheme is suitable for planar sections of a segmented volume, in order not to over sample data from the lower tilt angles nor under sample data from the higher tilt angles.[71]

After the data collection, any distorted images need to be removed and the remaining images need to be aligned. After the fine tuning of the alignment, the 3D structure of the imaged specimen can be reconstructed using a reconstruction algorithm based on the Radon transform[72].

ET has successfully been applied on hard porous materials: e.g. a porous low- dielectric[43], crystalline materials including a few voids[73, 74] and mesoporous silica-based materials[3, 75, 76]; and soft materials: e.g. block copolymers[77], polymer solar cells[9, 10, 78] and nanoparticles in a soft matrix. There are plenty ET studies of single complex objects, e.g. nanoparticles[44], nanoparticle aggregates or graphene dispersed in a polymer matrix[45–49]. The conceptual differences between particles dispersed in a polymer matrix, and a particulate hydrogel network structure is shown in figure 1.1. Hence, to my best knowledge, ET has not previously been used for the study of PSHs. Also, ET studies of other particulate hydrogels are few, if any.

2.4.1 Beam sensitivity and artefacts

All materials are more or less sensitive to the electron beam[79]. Due to the risk for beam damage, the total exposure time and voltage during a tilt series acquisition should be kept to a minimum, while still maintaining the amount of data required for sufficient quality of the reconstruction of the sample.

When imaging plastic embedded materials, it is especially important to have this in mind, since the most common form of beam damage is shrinking of the specimen in one or several of the spatial directions[79]. In the 3D case, this shrinkage can be seen as "y"-shaped features in the reconstructed sections, see figure 2.2, which affect the resolution of the tomogram. Another difficulty for plastic embedded materials is the risk of contamination. Especially in STEM mode, when the beam is repeatedly focused at one position between scans, there could be a build-up of hydrocarbons, distorting the contrast of the specimen locally or on a larger area.

In tomography, effects in the reconstruction appearing as a consequence of the data acquisition rather than the sample itself are denoted artefacts. The most common artefact in electron tomography originates from the Missing Wedge (MW), see figure 2.3 and 2.4. It originates from the specimen holder restraining the possible tilt range, meaning that information from the highest tilt angles is lost. High-tilt information can also be lost due to a decrease in image quality for higher tilt angles, see figure 2.3. The MW artefact results in the reconstructed tomogram having an elongation in the thickness direction, i.e. parallel to the electron beam at 0° tilt. Some tomo-



Figure 2.2: An example of how shrinking during tilt series acquisition may manifest itself in the reconstruction. The reconstructed particles are shaped like the letter Y. Screenshot from the Tilt Axis Adjustment step in Inspect3D, from a tilt series of Gel 1.

grams show streaking artefacts, which arise from the MW artefact in the y-direction. In one of the tomograms (figure 5.9), the particles are somewhat lemon-shaped. This phenomenon has recently been attributed to the point spread function[80].

Another factor having a large impact on the resolution and accuracy of the reconstructed structure is the alignment of the images in the tilt series. The tilt axis needs to be in the centre of each image, and the ever-present small horizontal holder movements need to be counteracted by image alignment. The images were aligned by a cross-correlation procedure in Inspect3D. Poor alignment will inevitably result in a poor structure reconstruction.

2.5 Mass transport

The process of movement of fluid, charges, particles or molecules are usually denoted as mass transport. Besides the structural factors, the properties of the transported molecules are also important for influencing the mass transport. For example, the ratio between the molecule size and the mesh size of the porous network has a large impact on the fluid transport. Other molecule parameters affecting the transport can be molecular weight, flexibility, charge and shape. Another material property affecting the mass transport is the surface chemistry of the pores, for example the hydrophobicity or hydrophilicity of the surfaces[81].

One example of the connection between function and mass transport is found in the process of controlled release, where for example a drug is to be transported out from a consumed tablet at the same time as water is transported in the opposite direction, for the purpose of obtaining an even release of the drug into the body of the patient over time[2].

A common denominator for the applications of porous soft materials is that the material function relies on the transport of water. It is often convenient to define the mass transport for a fluid in terms of diffusion and convective flow through the material[1]. In a previous study, liquid transport in a very heterogeneous emulsion was simulated in two dimensions using a finite element method based on structures obtained using confocal laser scanning microscopy micrographs[28]. Comparison of the simulated data with Nuclear Magnetic Resonance (NMR) data showed that the calculations underestimated the water diffusion on larger length scales, and the effect was attributed to the inherent three-dimensional connectivity in open porous structures. The authors suggested further evaluation of the dimensionality and connectivity using real materials, e.g. gels, where the structural information is available in both two and three dimensions[28]. Hence, information about the interconnecting pore structure in three dimensions is deemed especially important when predicting transport properties, since transport is a three-dimensional process[28]. The importance of transport in functional materials motivates the interconnectivity to be investigated further.

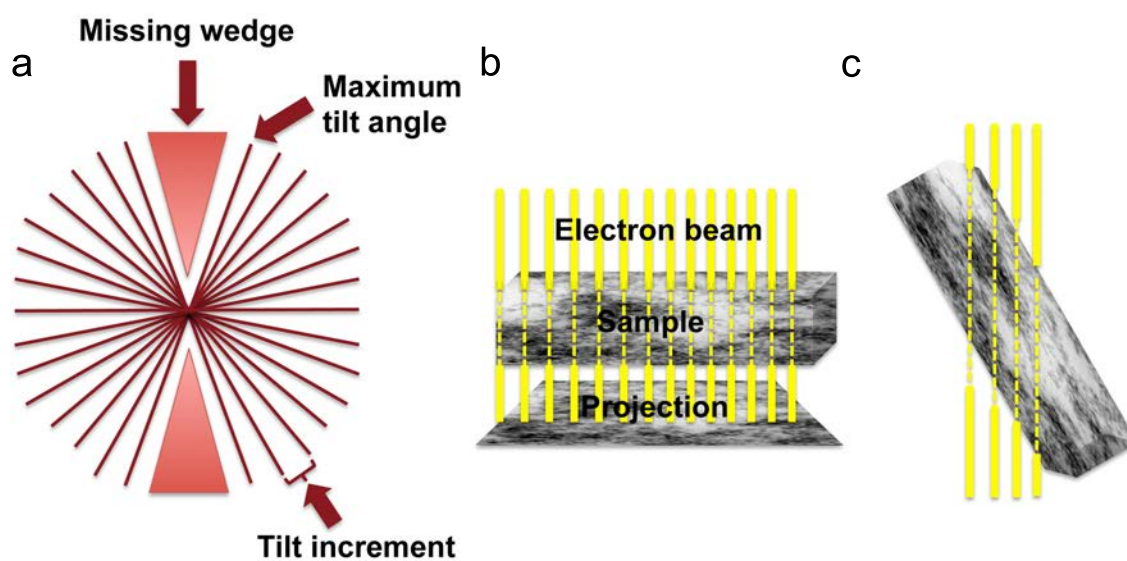


Figure 2.3: (a) During the tilting process, the specimen holder usually limits the tilt range. Information from the highest tilt angles will therefore be lost. This MW artefact manifests itself as the reconstructed tomogram having an elongation of features in the direction parallel to the electron beam at 0° tilt. (b-c) When the sample slice is tilted with respect to the electron beam, the distance travelled by the electrons within the material will be larger and the electrons will scatter more, resulting in a poorer image quality. This effect adds to the missing wedge effect, since images of too poor quality cannot be used for the reconstruction of the structure.

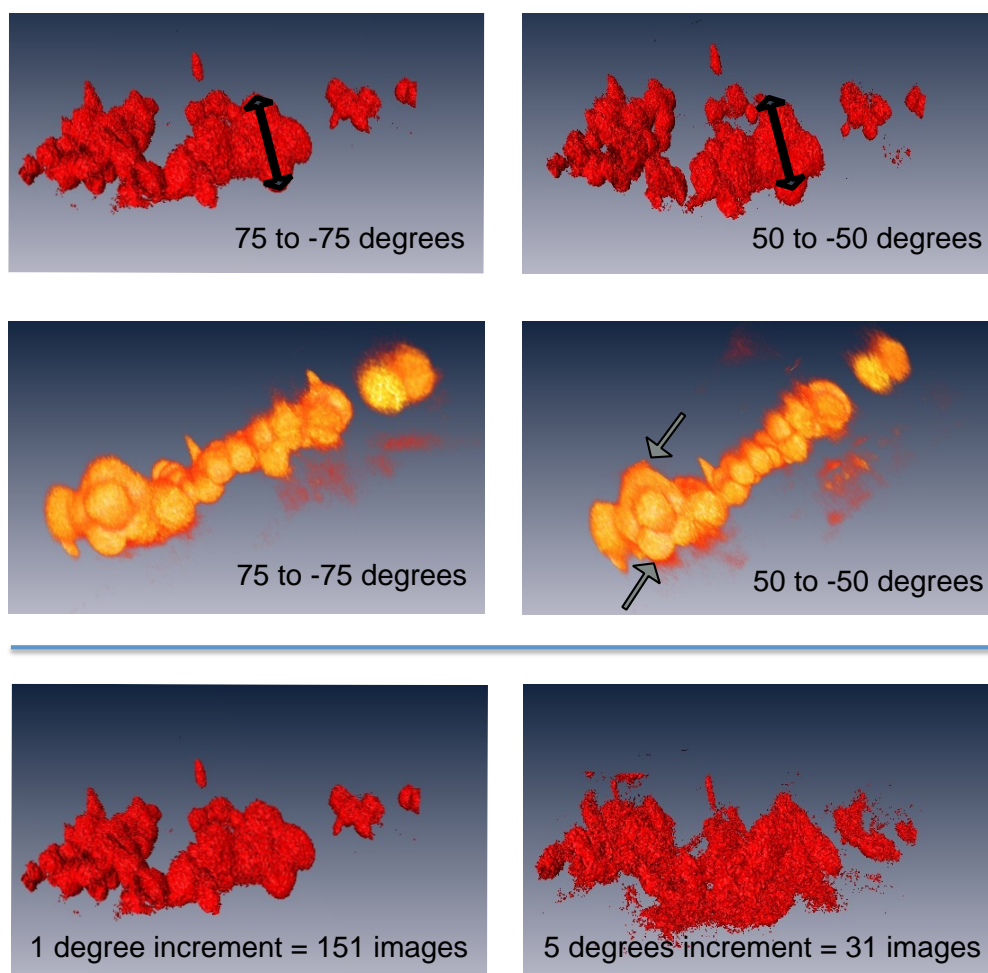


Figure 2.4: Examples of the elongation and flaring effects due to the MW artefact, and the image quality loss due to large increment between tilts. All images show high magnification constructions of a 70 nm slice of Gel 1 (particles approximately 20 nm in diameter), from ET on Titan at an operating voltage of 300 kV. The acquisition tilt range was $\pm 75^\circ$ to with a linear tilt increment of 1° . **Upper row:** Comparing the right and the left images, elongated structures in the missing wedge direction can be seen. The arrows have the same length. The particles are visualised by their isosurfaces. **Center row:** Comparing the right and the left images, flaring in the missing wedge direction can be seen. The arrows point to the most prominent flares. The particles are visualised by volume rendering. **Lower row:** Comparing the right and left images, poor particle definition due to too larger increment steps during acquisition can be seen. The particles are visualised by their isosurfaces.

2.5.1 Flow

When a fluid or particles are transported along for example a pressure gradient or a gravitational gradient, it is referred to as flow. For gravitationally-driven laminar flows through a porous material, Darcy's law describes the relation between total flow rate (Q) and the hydraulic permeability (κ) of the material, as

$$\kappa = -\frac{L\mu}{\rho gh}Q, \quad (2.2)$$

where ρ is the density of the liquid, g is the acceleration of gravity, L is the pillar height and h is the height difference determining the hydraulic pressure on the sample[25].

The Hagen-Poiseuille relationship,

$$Q = \frac{\pi R^4}{8L\eta}p, \quad (2.3)$$

is used for determining how well a pipe transports fluid. In this relationship, the pores are assumed straight, and the flow is steady and laminar. The flow rate (Q) is proportional to the pipe radius to the power of four (R^4), and inversely proportional to the pipe length (L). η denotes the fluid viscosity, and p is the pressure drop, driving the flow. As a consequence, for a specific pressure, the flow rate through larger pores will be much higher than for smaller pores. Thus, the importance of flow as the dominating mass transport mechanism is expected to decrease with decreasing pore radius. In comparison with Ohm's law the pressure drop is equivalent to the potential drop, which drives a current. According to the same analogy, the (hydrodynamic) resistance of the pipe is given by $\frac{8\eta L}{\pi R^4}$ [25].

The Reynold's number (Re) is a dimensionless ratio between inertial and frictional forces in a flow, and is used for characterising a flow as laminar or turbulent. It is defined as

$$\text{Re} = \frac{\mathbf{F}_{inertial}}{\mathbf{F}_{viscous}} = \rho \frac{vl}{\eta}, \quad (2.4)$$

where ρ and η represents the density and viscosity of the fluid respectively, and v and l denotes the characteristic velocities and length scales of the investigated system respectively[25]. In order for turbulent flows to occur, the Re is generally less than 2300[82].

2.5.2 Diffusion

Diffusion originates from the concept of Brownian motion of molecules. It is a random motion driven by the internal heat of the system. Diffusion is often discussed in terms of molecules having a net movement along a concentration gradient according to the second law of thermodynamics. Eventually the gradient will fade away, but the local movement of the individual molecule is not affected. If only one type of molecule is present, the diffusion is often referred to as self-diffusion, as is the case in this work.

The interactions between the fluid and the solid network structure are very rapid, and the diffusion properties are determined by a variety of factors. There is still no unified theory predicting the particle movements in all categories of structures, instead there are several models, all optimised for certain type of system[83]. Factors affecting the diffusion are for example the obstruction by the solid network structure, the hydrodynamic and the thermodynamic interactions (e.g. pore discontinuities or interface interactions)[84]. Hence, both the surface area and the accessible volume fraction are important factors influencing the diffusion properties. Simulations of tracer diffusion in colloidal gels have shown that the diffusion properties are mainly determined by the volume fraction accessible to the solute[85].

A useful quantity for evaluating the length scale in relation to flow and diffusion is the Peclét number (Pe). It is defined as

$$\text{Pe} = \frac{vd}{D}, \quad (2.5)$$

where v can denote the flow speed through the material, d denotes the characteristic length scale or length of the system, and D is the diffusion coefficient of the medium (within the porous sample). If the Pe number is larger than one, flow is dominating, and if it is smaller than one, diffusion is dominating[25]. In this work, we investigate systems where the Pe number is close to one.

2.5.3 Pressure driven flow speed measurements (porosimetry)

In analogy with Darcy's law (equation 2.2), the flow rate through a sample can be determined using porosimetry, which is referred to as *Falling-head test* in **Paper II** and by Abrahamsson *et al.*, 2014[11]. The procedure was introduced in the 80's[86, 87] and has since been used for e.g. determining the permeability and flow rate of particulate hydrogels[11, 88]. The principle in such a test is to subject a column of hydrated porous material to a small pressure gradient originating from an applied hydraulic pressure (water column). As the water penetrates the porous material, the height of the water column decreases. By finding the slope from plotting the height level of remaining water as a function of time, the total flow rate Q can be determined. It is important to balance the measurements concerning evaporation and to remember that the pressure itself also decreases as a function of time.

2.5.4 NMR diffusometry

A method that provides a non-invasive, convenient, multi-component substance selective method for measuring translational motion is NMR diffusometry. It provides information about the global diffusion properties in basically any type of liquid-like material. Diffusion coefficients as small as 10^{-17} m²/s may be observed with good accuracy during optimal conditions. The Larmor frequency is dependent on the magnetic field. In NMR diffusometry, a magnetic field gradient is applied. Thus, the Larmor frequency reports about the spatial position of the molecules. During diffusion, the molecule passes areas with different magnetic fields due to the gradient. The phase shift of the Larmor frequency can be correlated to the diffusion rate[89], and a diffusion coefficient can be extracted.

Chapter 3

Experimental

3.1 From colloid to electron microscopy sample

One common denominator for **Paper I-VI** is the material studied, PSHs. Several PSHs were prepared from suspensions of colloidal silica nano-particles. Three samples were chosen for detailed study, each constituted from a different particle of unique size and morphology. This section describes the particulate silica gel samples, and the preparation of them for electron microscopy.

3.1.1 Particulate silica hydrogel preparation

The three PSHs were constituted by nanoparticles of a certain size per gel, and were prepared from colloidal suspensions of amorphous silica¹[6, 90]. Two of these suspensions contained pre-aggregated nanoparticles, see table 3.1. The solid volume fraction of the PSHs was 9.0wt% for all samples. The particles and the gels are further described in **Paper I**.

Table 3.1: Preparation parameters for the three particulate silica hydrogels. The initial pH of the sol is denoted Init. pH, and the pH after adjustment is denoted Adj. pH.

Name	Sol	Pre-aggr.	Doping	Init. pH	Adj. pH	[NaCl]	wt%
Gel 1	Bindzil 40/130	No	No	9.1	7.8	0.5 M	9.0
Gel 2	Bindzil 15/500	Yes	No	10	7.0	0.9 M	9.0
Gel 3	GB3000 and 0.4wt% Bindzil 40/130	Yes	Yes	11	7.0	0.9 M	9.0

The PSH preparation was initiated by a pH decrease of the colloidal suspension, using Dowex Marathon C². The pH decrease was immediately followed by Dowex Marathon C removal using suction filtration. Ultra-pure de-ionized water and NaCl were added to the filtered sols, adjusting the concentration of silica and NaCl (table 3.1). The GB3000 solution was doped with an additional 0.4 wt% of Bindzil 40/130. The colloid silica particle sizes and configurations were: Bindzil 40/130: isolated particles of 22 ± 5.0 nm; Bindzil 15/500: pre-aggregated particles with an initial particle size of 5.0 nm; GB3000: pre-aggregated particles with an initial particle size of 3.6 nm. Finally, the mixtures were shaken in a vortex shaker, and left to gel. The resulting gel structures had pore-size averages as follows: Gel 1: 310 ± 180 nm; Gel 2: 58 ± 32 nm; Gel 3: 18 ± 15 nm (data acquired by circle-fitting, see **Paper I**).

¹Provided by AkzoNobel Pulp and Performance Chemicals AB

²Sigma-Aldrich Co. LLC, Saint Louis, MO, USA



Figure 3.1: (a) The gel samples were prepared in glass vials with a diameter of 24 mm. A scalpel was used for cutting $1 \times 1 \text{ mm}^3$ gel samples for plastic embedding. Samples were retrieved from the bulk part of the gel, where no surface effects were likely to occur. (b) The three different gel samples, here contained in NMR tubes. Large differences in opacity can be seen. From top to bottom, the sample order is: Gel 1, 2 and 3.

According to Mie theory, structures of a comparable size to visible light will scatter more as function of diameter of the scattering object[91]. In this case the scattering objects are the pores, since they are of a comparable size as the wavelength of visible light. The same phenomenon has been confirmed for several porous structures, e.g. in amelogenin gels[92]. These scattering differences are present in colloidal silica gels, and can clearly be seen in figure 3.1b, confirming the statement above. Here, Gel 1 has the coarsest pore network (both in pore size and particle size) and Gel 3 has the finest network.

3.1.2 Dehydration, infiltration, embedding and thin sectioning

In order to prepare samples for the high-vacuum condition in electron microscopy, the water within the hydrogels was carefully replaced with a resin³: millimetre sized cubes were isolated from the inner volume of the gel sample, and was subsequently infiltrated with the low viscosity resin. This infiltration technique [93, 94] is standard procedure in life science. The gel cubes were dehydrated by immersion in a series of ethanol solutions of escalating ethanol percentage (*i.e.* a graded ethanol series) ending at 99.5% ethanol, followed by a graded propylene oxide series and a graded resin series ending at a pure resin solution. The graded ethanol series was used for preventing sample shrinkage. In the case of a small amount of shrinkage, it is assumed to be isotropic[12]. Any shrinkage would have presented itself already after the infiltration process, and no such indications were detected for the silica gels.

After the infiltration process, the silica cubes were embedded in plastic blocks for easier handling during the sectioning process. A large challenge during sectioning was that both the silica samples and the embedding plastic were clear and transparent, making the silica gel difficult to locate within the block. I solved this problem by covering the plasticised silica sample in talcum powder immediately prior to the embedding, making the edges of the embedded gel cube more prominent.

Thin sections of between 70 nm and 200 nm were generated using a PowerTome XL⁴ and a diamond knife⁵, see figure 3.3. The sections were placed on 200-mesh carbon support film Cu-grids⁶.

³TLV (TAAB Laboratories Equipment Ltd., Berks, England)

⁴PowerTome XL (RMC products, Boeckeler Instruments Inc., Tucson, Arizona)

⁵DiATOME, Biel, Switzerland

⁶C101/100 (TAAB Laboratories Equipment Ltd., Berks, England)

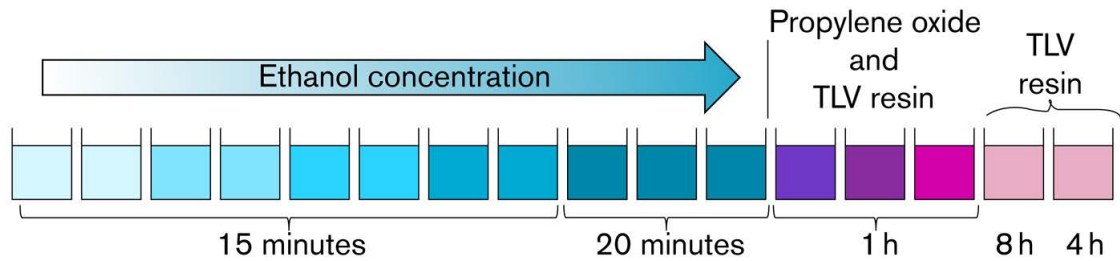


Figure 3.2: Schematic representation of the plastic embedding process. The samples were embedded in resin by dehydration in a graded series of ethanol, propylene oxide and resin. In an automated carousel, the gel cubes were subsequently treated with each of eleven solutions of ethanol (ranging from 30% to 99.5%) followed by two submersions in 100% propylene oxide, and two steps of ascending resin concentrations up to the last step of pure resin. The NaCl concentration in the ethanol solutions was kept at the same level as in the respective gels for ethanol concentrations of up to 70%.



Figure 3.3: An ultramicrotome with a diamond knife and a water tray was used for the thin sectioning of the samples (thickness from 70 nm and up). The thin sections were collected from the water surface onto 200-mesh copper grids with a carbon support film. Photos: Dick Gillberg, courtesy of SP Food and Bioscience.

3.1.3 Freeze fracture and freeze etching

It is crucial to ensure that the sample preparation affects the structure of the material as little as possible. The effect of sample preparation can be evaluated by comparing the result of more than one sample preparation technique. As a complement to the plastic embedding, the freeze-fracture and freeze-etching methods[95] were used for comparison. In short (see figure 3.4), the sample is plunge frozen in liquid propane ($-196\text{ }^{\circ}\text{C}$), fractured at a temperature of $-100\text{ }^{\circ}\text{C}$, etched for two minutes and shadowed with platinum and carbon. The obtained replica is then removed from the original sample.

As a small control experiment (Figure 3.5), a comparison between freeze-fracture freeze-etching preparation and from plastic embedding of the gels was performed. Since the freeze-etched replica represent the surface topography of a freeze fractured and freeze etched gel sample, it stands in contrast to the embedded and thin-sectioned samples, where the images are projections of the sample. In the projected TEM images, an apparent pore structure is easily seen, but it is important to remember that this structure will be affected by the section thickness. The comparison show that the characteristic length scale within the sample, the shape and the connectivity of the structure seems to be independent of preparation technique, and no signs of sample shrinkage during plastic embedding can be seen. I used plastic embedding[93, 94] for all samples studied by 2D imaging or ET which also in other studies of similar materials, was used without any indications of the structure being affected[12].

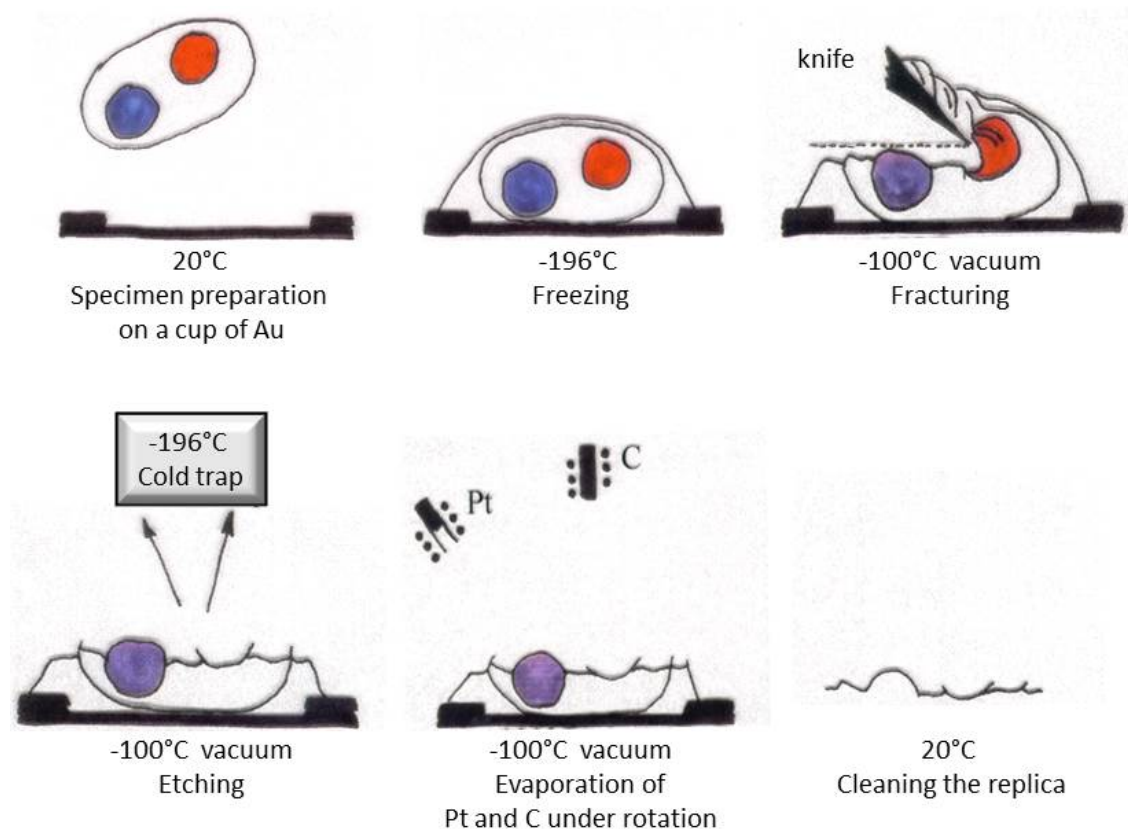


Figure 3.4: Schematic image of the procedures of freeze fracture and freeze etching. Image courtesy of Annika Altskär, SP Food and Bioscience.

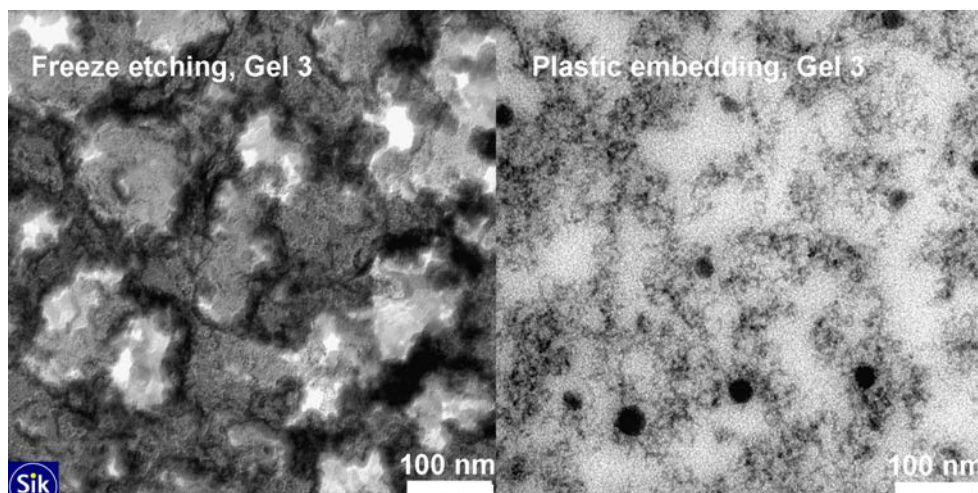


Figure 3.5: A comparison between a plastic embedded Gel 3 specimen and freeze fractured replica of the corresponding sample. A comparison between the freeze etching and the plastic embedding methods, illustrating both the similarities in structure detected using the two methods, and the challenge of a quantitative comparison of the two techniques. In the freeze etched sample, the light grey and white areas correspond to the light areas in the plastic embedded sample. The darker, more evenly grey structures in the freeze etched sample, visualises the aggregated silica structure, which can be seen as the darker structure in the plastic embedded sample. When taking the differences in the two preparation techniques into account, no apparent differences in material structure can be detected between the two preparation techniques.

3.1.4 Sample selection based on porous length scale

Three PSHs were selected based upon the length scale of their porous network structure, in order to reflect a range of length scales spanning from a diffusion dominated region to a region dominated by viscous flow. The gels were chosen for detailed characterisation of their porous nanostructure, and their flow and diffusion properties. The structural characterisation was performed in both 2D and 3D.

The selection of these gels was based on an initial screening of the approximate pore sizes of the gels. The pore size estimation was performed using TEM images of equal sample thickness of the embedded gels, and manually positioning four to five circles into the images in a way that the circles were drawn as large as possible without overlapping any areas of silica structure. This procedure was repeated for a few images of each sample and the pore size estimation was then defined to be the median diameter of the circles for each sample. The data for all samples are presented in table 3.2.

Since diffusive mass transport can be considered a function of the volume accessible to the solute[85], the silica solid volume fraction of the gels was also considered when selecting the samples.

Table 3.2: Pore size estimation chart. The three selected gels are marked in italics, and have a silica percentage of 9.0 wt%. The sphere diameter data is from Abrahamsson et al.[11]^a and AkzoNobel, PPC AB^b.

Product name	Est. pore size [nm]	Particle diameter [nm]	SiO _x	pH	[NaCl]
Bindzil 40/130	500 nm	22±5 ^a	9.0 wt%	7.8	0.9 M
<i>Bindzil 40/130</i>	<i>430 nm</i>	<i>22±5^a</i>	<i>9.0 wt%</i>	<i>7.8</i>	<i>0.5 M</i>
Bindzil 40/130	430 nm	22±5 ^a	9.0 wt%	4.0	0.9 M
Bindzil 40/130	430 nm	22±5 ^a	9.0 wt%	4.0	0.5 M
Bindzil 40/130	370 nm	22±5 ^a	5.0 wt%	7.8	0.9 M
Bindzil 40/130	240 nm	22±5 ^a	5.0 wt%	7.8	0.5 M
Bindzil 30/360	150 nm	7 ^b	9.0 wt%	7.0	0.9 M
GB3000	145 nm	3.6 ^b	6.0 wt%	7.0	0.9 M
<i>Bindzil XP1</i>	<i>130 nm</i>	<i>5.0^b</i>	<i>9.0 wt%</i>	<i>7.0</i>	<i>0.9 M</i>
<i>GB3000</i>	<i>60 nm</i>	<i>3.6^b</i>	<i>9.0 wt%</i>	<i>7.0</i>	<i>0.9 M</i>

3.2 Transmission electron microscopy studies

The TEMs used for imaging the ultramicrotomed sections were

- a Titan 80-300 Field Emission Gun (FEG) (FEI Company, Eindhoven, Netherlands) operated at an acceleration voltage of 80 kV or 300 kV,
- Tecnai G2 LaB₆ (FEI Company, Eindhoven, Netherlands) operated at an acceleration voltage of 200 kV,
- a Leo 906E with a tungsten filament (former LEO Electron Microscopy Ltd, now Zeiss, Oberkochen, Germany) operated at an acceleration voltage of 80 kV.

3.2.1 ET on particulate silica hydrogels using STEM

Conventional TEM and STEM imaging create only a 2D projection of the 3D material, where important information concerning actual size of the pores, pore interconnectivity and shape of connecting features, are not directly accessible. This means that a full characterisation of the transport paths, as well as the distribution and sizes of pores is not possible using only data from 2D imaging.

Although the principle of tomography itself is fairly straight forward, retrieving high resolution tomograms is demanding since it requires careful sample preparation, imaging of a possibly beam sensitive sample with low contrast, image alignment using cross correlation, reconstruction and visualisation. In this work, ET was used to image colloidal silica nanoparticle gel samples with different pore sizes. The tilt series acquisition was performed in STEM mode, since our earlier studies within this work showed that STEM provided better signal-to-noise ratio, higher contrast and sharper focus. This agrees well with suggestions from literature[67, 69].

For the collection of the tilt series, the Advanced Tomography Holder Model 2020 (E.A. Fischione Instruments, Inc., Export, PA, USA), a specially adapted single tilt holder, was used, enabling a tilt range between +80° to -80°. The Saxton imaging scheme[71] was used, since the sample was planar segments of a volume. The software Xplore3D and Inspect3D (FEI Company, Eindhoven, Netherlands), and occasionally IMOD[96] were used for image acquisition, cross-correlation alignment and reconstruction of a 3D volume from within the specimen. The resulting reconstructions were visualised and if necessary, filtered and thresholded, using Amira 5.3.2 and Avizo 8.1 (both from Visualization Sciences Group, an FEI Company).

When imaging the single silica nanoparticles, a higher voltage could contribute to altering the particle shape. Hence, when imaging the single particles of Gel 2 and 3, a lower voltage of the electron microscope was used (80 kV on the Titan).

3.3 Mass transport measurements

3.3.1 Porosimetry on particulate silica hydrogels

Here, the flow through the porous material is driven by a pressure gradient. Open-ended test tubes were used to measure the steady state flow speed of the silica gel as previously described[11, 87].

The gel samples were gelled in open-ended borosilicate glass tubes with an 8 mm inner diameter. The gel was resting on a polyester mesh in order not to escape from the glass tube. The total height of the gel sample within the glass tube was 30 mm, and the meshed end was in contact with the bottom of a Petri dish filled with 0.9 M NaCl solution of 8 mm depth. The column was filled with 50 mm of 0.9 M NaCl aqueous solution on top of the gel. The flow rate through the gel was measured by marking the position of the liquid surface, one to two times a day. A parafilm seal, slightly perforated to eliminate underpressure, made evaporation from the top of the column insignificant. Petri dishes were replenished by MilliQ water every day to compensate for water evaporation and all experiments were carried out at room temperature. The salt concentration of the gels was adjusted to the same level for all samples, in order for the ionic strength not to interfere with the permeability tests.

3.3.2 NMR diffusometry on particulate silica hydrogels

The self-diffusion coefficients of the three PSHs were measured one to two weeks after gelation, using a Bruker Avance 600 spectrometer (Bruker, Karlsruhe, Germany) and a Diff30 diffusion probe with a maximum gradient strength of 1200 G/cm. These diffusion measurements were performed with support from the Swedish NMR centre.

Chapter 4

Data analysis and computer simulations

The term porous materials includes all variations in-between materials with isolated pores (voids) and materials where all voids are interconnected. A pore network can have a varying pore diameter and multiple branches. However, the definition of a pore is not as straight forward as it might seem. We have used two different analysis methods for determining the pore size: a stereological a geometrical approach. For the pore morphology, a skeletonisation in three-dimensions was performed. We also used the maximum log-likelihood approach for creating a simulated micrograph in 3D from a 2D micrograph, this approach is outlined in this chapter. The principles of ET post processing is also explained here. Finally, the data analysis concerning interconnectivity, accessible pore volume fraction and mass transport analysis is presented.

4.1 Image analysis

4.1.1 Stereological pore size analysis

Stereology is a mathematical and statistical method for determining 3D characteristics from 2D data. The strength of this method is the use of a mathematically defined description of a pore, regardless of its morphology. The development of the techniques started in the 1960's, but the mathematical mindset of geometrical probability goes back several hundred years. Due to the relative ease in acquiring large quantities of 2D images, compared to 3D ones, the stereology approach is often used for finding microstructural information in e.g. food science[97] and medicine[98]. These methods are also widely used in the area of pathology[99],[100] and have also successfully been used for the characterisation of e.g. kinetically trapped phase separated biopolymer mixtures[101].

Stereology provides theoretically unbiased statistical methods for estimating the volume of arbitrarily shaped structures (based on 2D images)[102]. In this work, stereology was used for estimating the pore size of the different silica gel samples.

The Volume-Weighted Mean Volume (VWMV) is an unbiased estimator, where no assumptions of particle or pore shape have to be made[103]. The only requirement is that the sections are recorded from randomly chosen regions, and that the material is geometrically isotropic. The input data should ideally be an infinitesimally thin section from a 3D structure. Using this estimator, we also define the concept of a pore. Since the method is volume weighted[102], it is well suited for use within mass transport studies.

The definition of the stereological estimator: VWMV, also called "star volume", is stated in Gundersen *et al.*[99] as "the mean volume of all parts of an object that can be seen unobscured in all directions from a particular point". Hence, the VWMV is condensed to one single mean value for the structure. The VWMV is calculated as

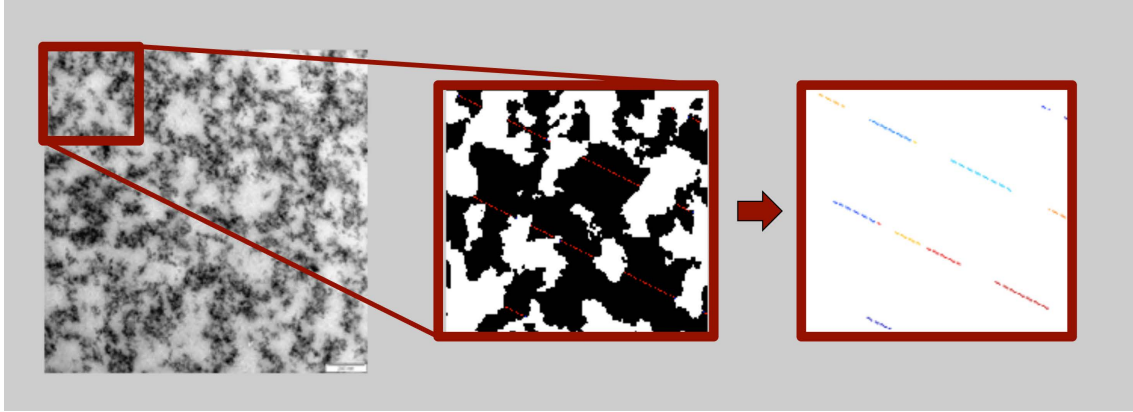


Figure 4.1: Illustration of key concepts in star volume estimation of pore volume. The projected (S)TEM image is binarised and intercepts (superimposed thin red lines) are introduced with 200 pixels spacing. The isolated intercepts are shown in colour for clarity.

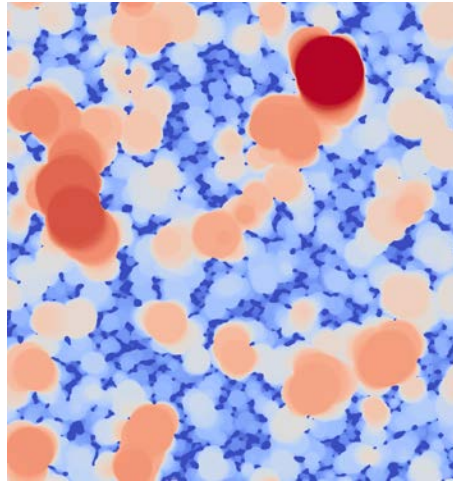


Figure 4.2: From a geometrical point of view, the pore sizes are determined by the largest sphere that can surround each pixel without touching the structure. This approach allows for a pore size distribution to be presented.

$$V^* = \frac{\pi}{3} l_0^3. \quad (4.1)$$

Here, V^* denotes the VWMV and l_0 denotes the intercept length, i.e. the length of an intercept randomly passing through a void within the sample, see figure 4.1.

The interfacial area (S_V) of the silica surface of the pores were also estimated using stereology. This area can be determined as

$$S_V = 2 \frac{P}{l_0}, \quad (4.2)$$

where P/l_0 denotes the numbers of intersection points per intercept length[97].

2D images of approximately 70 nm thick sections of the embedded silica nanoparticle gels were used. Because of the specimen thickness, the VWMV is underestimated. For the quantitative analysis, the TEM or STEM images (grayscale) were converted to binary images, by a series of filter steps performed in MATLAB (The MathWorks, Inc., Natick, MA, USA).

4.1.2 Geometrical pore size distribution analysis

The geometrical analysis was used in **Paper II** and **Paper V** for determining the pore size distribution (Pore Size Distribution (PSD)) and the arithmetic mean diameter (Arithmetic Mean Diameter (AMD)) of the pore network. In this approach, circles or spheres were fitted into the pore volume in two and three dimensions, respectively. For clarity I will describe the example as a sphere-fitting technique. The operation was performed in order of sphere size until no pore volume remained. If a voxel in the binary structure had no material, a sphere as large as the structure allows without intrusion into the material was inserted. This was done for every voxel and the spheres were inserted in order of decreasing diameter, until the sample volume was completely filled, see figure 4.2. Subsequently for each voxel, the diameter of the largest sphere enclosing it was obtained and the number of voxels paired with a certain sphere diameter were plotted in a histogram. This method is area weighted in two dimensions and volume weighted in three dimensions. Hence, the mean of the distribution gives an area weighted or volume weighted measure of the average pore size, AMD.

The analysis was performed in MATLAB, either on a series of projected images of 90 nm thin sections (as in **Paper II**), or on the tomograms (as in **Paper V**). The resulting histograms are presented as the fraction of the total number of pixels or voxels which correspond to a circle or sphere of a certain size.

4.1.3 Pore morphology by skeletonisation

In **Paper V**, the pore volume was also described by the pore skeleton, which provides another morphological aspect to the pore characterisation. Skeletonisation procedures in two dimensions often use thinning algorithms for attaining the structure depicted as line segments. With mass transport in mind, we were especially interested in the presence and size of pore throats which connected larger open regions. Hence, a three-dimensional watershed transform in MATLAB was used for obtaining the pore space skeleton. Primarily, the distance from each pore voxel to its nearest material voxel was detected, and this value was assigned to each voxel, creating a *Euclidean distance map*. A watershed transform then identifies the ridges of this Euclidean distance map, creating basins. The extracted skeleton corresponds to the watershed lines separating these basins. Each voxel in the skeleton was then assigned its Euclidean distance value, thus labelling the skeleton. From this labelled skeleton, the information about the pore throats (which we define as local minima in the labelled skeleton) are extracted.

By a nearest-neighbor analysis of the pore skeleton (which also includes *faces*), the complexity of the pore volume could be shown in a histogram. A pore voxel can have maximum 26 neighbouring voxels. Branching points and face points in the skeleton cannot be identified uniquely using this method, since the number of neighbours can vary from three to ten. However, a comparison based in this data can still be valuable. These histograms for the three particulate silica gels were compared, and it was found that they were very similar in this sense.

4.1.4 The maximum log-likelihood method for 3D simulations from 2D images

A statistical approach based on the log-likelihood of the response observed at each pixel was used when investigating the intensity in 2D projections as a function of mass thickness (i.e. the fraction of silica in the direction of the electron beam, for each pixel in the image). The intensity function

can be estimated as e.g. linear or as a power law. Here, the power law is chosen to illustrate the estimated function.

When estimating the intensity (I) as a function of silica mass thickness (α), there are several unknown parameters that need to be estimated: the background intensity of the image (b), the power constant of the function (β), and a constant c . The equation can then be presented as

$$I(\alpha) = b + c\alpha^\beta, \quad (4.3)$$

and is specific for each pixel. Since α denotes the mass thickness of the investigated simulated micrograph, it also includes the underlying information of the particle positions and the number of particles, although it is not explicitly written in the equation.

The next estimation step is the particle centre positions, which are denoted $[\mathbf{x}_0, \mathbf{x}_1, \dots, \mathbf{x}_N]$, and the number of particles (N). A normally distributed noise term is finally added as a factor in the intensity function (equation 4.3), and the variance (σ), of this noise term also needs to be estimated.

In general, when estimating the expectation of normally distributed observations using a log-likelihood approach, the estimation can be obtained by determining the maximum of the log-likelihood function, which is the same as the arithmetic mean of the observations. However, there is not always an analytical solution available, especially when a large number of parameters is involved. This is the case for the intensity estimation used here, where the log-likelihood function (l) summed over all pixels (n), is given by

$$l(N, \beta, \sigma, b, c, \mathbf{x}_0, \mathbf{x}_1, \dots, \mathbf{x}_N) = -n \log(\sqrt{2\pi}\sigma) - \sum_{i=1}^n \left(\frac{1}{2\sigma^2} (I_{0i} - I_i)^2 \right) \quad (4.4)$$

which requires a numerical maximization [104]. Here, I_{0i} denotes the intensity value for that particular pixel in the original micrograph, and $n = |M|$ in **Paper I**.

In this approach, circular discs representing the particles were positioned within an image frame before maximizing the log-likelihood function to estimate the mentioned variables. After this step, the log-likelihood function was maximized again, after changing the positions of the discs. Iteration between these two steps was performed until a maximum was reached. The maximum likelihood approach can be used generally for estimating an intensity relationship to STEM micrographs when some information of the underlying geometry or topological features are known.

4.1.5 Ripley's K -function

Within spatial statistics, the summary function used in **Paper III** and for the 2D - 3D comparison in the aggregation dynamics part of this work is Ripley's K (or L)-function, see section 5.3. Ripley's K -function a tool for analysing a constellation of points[105] (e.g silica nanoparticles). Hence, it was used for quantifying the particulate silica hydrogel structures and comparing it with RLCA modelled data. Ripley's K -function (without edge-correction) can be estimated as[105]

$$\hat{K}(r) = \lambda^{-1} \sum_i \sum_{j \neq i} I(d_{ij} < r) / N. \quad (4.5)$$

The output $\hat{K}(r)$, provides information about the distribution of internal distances (d_{ij}) between all possible point-pairs in a sample of N points. λ , the average density, is often defined as the the number of points per area unit, or N/A , in the whole sample. If the points are clustered, this will show up as maxima when plotting K as a function of the distance r .

The L -function is a version of the Ripley's K -function which is used for data analysis, and is estimated as[105]

$$\hat{L}(r) = \sqrt{\hat{K}(r)/\pi}. \quad (4.6)$$

4.2 Principles of ET post processing

4.2.1 Image alignment

It is of great importance to align the images in the tilt series with high-precision. The common tilt axis is placed in the center of the image series during this marker-less alignment procedure, performed in Inspect 3D, FEI. This alignment is done by a semi-automatic built-in cross-correlation alignment procedure of the images. The procedure of cross-correlation based image alignment starts with optional stretching of the images. The stretching can improve or worsen the alignment, so this is a matter of testing by the user. The images in the series are then Fourier transformed, and filtered using high and low-pass filters (adjusted by the user). The in-depth details of the cross-correlation automation are described elsewhere[106], and will not be explored further here. After the cross-correlation, the images are inversely Fourier transformed and a correlation peak arises, which should be as narrow as possible. The images are usually correlated in pairs, whereafter the global shifts are automatically calculated from the local shifts[106].

4.2.2 Reconstructing the tomogram

The mathematical solution for finding the 3D reconstruction from projections was found as early as 1917 by Radon[72]. However, the computational power needed for performing the necessary calculations for structural reconstruction has only been around for approximately 40 years[65].

In order to reconstruct the imaged object, the Radon transform is used. The details of the Radon transform are presented in the 1917 article by Radon[72]. The general principle of the Radon transform, however, is usually explained as going from one to two dimensions, which is equivalent to going from 2D to 3D. The Radon transform (R) is then a mapping of a function $f(x, y)$, which describes a real space object (D) by the projection, or line integral, through f along all possible lines L with unit length ds ,

$$R = \int_L f(x, y) ds, \quad (4.7)$$

see figure 4.3 for clarification. In practice, the set of all 2D images collected during a tilt series in the STEM can be seen as a discrete sampling of the Radon transform. Hence, using the inverse Radon transform on the projections will result in a reconstruction of the imaged object if the sampling frequency is high enough[67]. The inverse Radon transform is the foundation of the different direct algorithms available for tomographic reconstruction.

There are several different reconstruction algorithms[65]. Two of the most common ones are the Weighted Back-Projection (WBP) and the Simultaneous Iterative Reconstruction Technique (SIRT) algorithms. In this work, the SIRT algorithm was used since it is more accurate than the WBP method. The SIRT algorithm changes the densities of the reconstructed object by using all the projected images simultaneously. As the next step, the mean density value of the original object is compared to the mean density of the volume under reconstruction, and the reconstruction values are scaled in order for its mean density to coincide with the mean density of the original. These steps are repeated iteratively[107]. SIRT is one of the reconstruction algorithms embedded in the Inspect3D software, and is used in this work.

4.2.3 Visualising the tomogram

After the reconstruction of the tomogram is finished, the data needs to be visualised by segmentation. This is the process which determines which parts of the tomogram should be interpreted as structure and vice versa. The segmentation of the complex structure of the PSHs would have taken an unproportional amount of time and effort to perform manually, hence we used a global threshold for segmentation. The challenge of segmentation was recently outlined and a machine

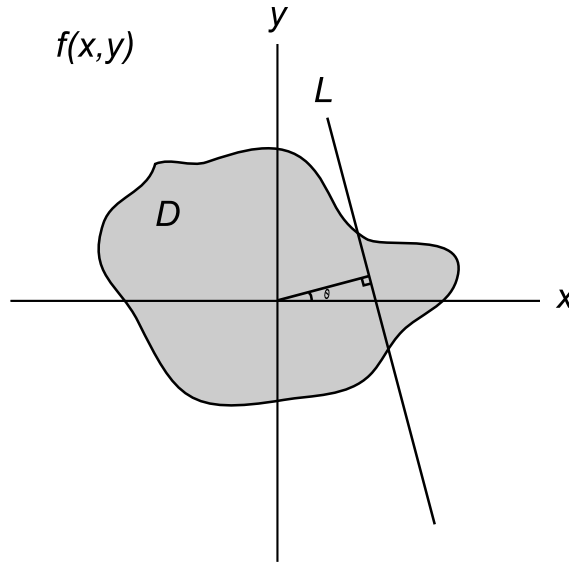


Figure 4.3: An illustration of the principle of the Radon transform (from 1D to 2D). D is the object to be reconstructed, displayed in a cartesian coordinate system representing real space. The line L shows just one representation of a line integral (equivalent to a projection), through the object D . The Radon transform can be visualised as the integration through D along *all* possible line integrals, L , at a specific angle θ to the x -axis.

learning algorithm was proposed and demonstrated[108]. However, this is a research field on its own and is beyond the scope of the present thesis.

4.3 Interconnectivity and accessible pore volume fraction analysis

In **Paper IV**, we determined the interconnectivity and accessible pore volume fraction of the pore network using a geometrical algorithm[109]. We defined the available pore volume as the part of the pore volume where an imaginary probe can fit. The accessible pore volume is then the part of the available pore volume that can be reached by the probe from the edge of the geometry. We defined the accessible pore volume *fraction* as the accessible pore volume divided by the total pore volume. The accessible pore volume fraction provides information on to what extent a probe of a certain size has access to the structure.

The interconnectivity is defined as the accessible pore volume divided by the available pore volume, also for an imaginary probe. It provides information on to what extent the pore network is connected on a certain length scale. The interconnectivity was determined by first using a mathematical morphological opening operator on the pore space of the thresholded three-dimensional structures, in order to compute the pore volume available to the probe of a specific size. The accessible part of the available volume was subsequently determined using a flood fill algorithm from four sample edges. This analysis was performed in MATLAB.

There is a critical thickness for each sample determined by its scattering properties (e.g. by the volume fraction of silica), sample section thickness and the contrast mechanism used for ET imaging, which we have handled the challenge of critical thickness by extending the tomograms to larger volumes by either mirroring[110] the structure or stacking them periodically.

4.4 Mass transport analysis

4.4.1 Flow speed determination from experimental data

The analysis of the flow speed measurements was performed in MATLAB, using linear regression analysis on the liquid pillar height data of the first 13 days for Gel 1 (after which the correlation could no longer be considered as linear), and the first 27 days for Gels 2 and 3. The values were calculated as a mean value from all the replicates (eight replicates for Gel 1, three replicates for Gel 2 and five replicates for Gel 3). Since the water pillar decreased in height, the pressure driving the flow was also decreasing. This is what causes the pillar height as a function of time to deviate from the linear relationship described by the Hagen-Poiseuille relationship, equation 2.3. The standard error, S , of the flow speed measurements was calculated using the MATLAB function `std`, which corresponds to

$$S = \sqrt{\frac{1}{1-N} \sum_{i=1}^N |A_i - \bar{A}|}, \quad (4.8)$$

where N is number of replicates and A_i is the value of index i in the vector A .

4.4.2 Lattice Boltzmann models (LBM) of flow and diffusion

LBM is an simulation technique for length scales in-between the atomic and purely classical length scales, and can be used for mass transport simulations. In contrast to conventional complex fluid dynamics methods (which is used on the classical length scale), where the conservation equations for macroscopic properties are solved numerically, LBM simulates the mass transport using a lattice mesh. In this lattice mesh, the movements and collisions of particles (representing the fluid) is simulated by using simplified kinetic models[83].

In **Paper V**, the tomograms from the ET was used as templates for the LBM flow simulations. The method used in **Paper V** solves the Stokes equations for low Reynolds number flow with non-slip boundary conditions on the structure boundaries. For each structure, the permeability κ was computed from Darcys law (equation 2.2). The mirrored or periodic boundary condition was used for expanding the sample volumes, as in the interconnectivity analysis. The software used was GESUALDO.

Chapter 5

Summary of results and discussion

In this chapter, the main results from **Paper I-V** are described and discussed. These results concern three main themes: i) the structure determination of particulate silica hydrogels in 2D and 3D, ii) mass transport from a nano-structure perspective and iii) application of the experimental structural data in aggregation dynamics studies.

Using the tomograms reconstructed from ET tilt series, we characterised the three-dimensional pore network in terms of fractal dimension, pore size distribution, pore morphology and pore interconnectivity. For mass transport studies, the convective flow and diffusion through the gels were simulated by LBM, using the tomograms as an *in situ* template for the simulations.

5.1 PSH structure in 2D and 3D

This section summarises the results concerning the structure determination of the primary silica nanoparticles and the three different gels, each constituted from one of the three silica nanoparticle types.

5.1.1 Primary particles

I take the opportunity to remind the reader that Gel 1 is constituted from Bindzil 40/130 particles, Gel 2 is constituted from Bindzil 15/500 particles and Gel 3 is constituted from GB3000 *and* Bindzil 40/130 particles. Bindzil 15/500 is denoted as "Bindzil XP1" in **Paper I**.

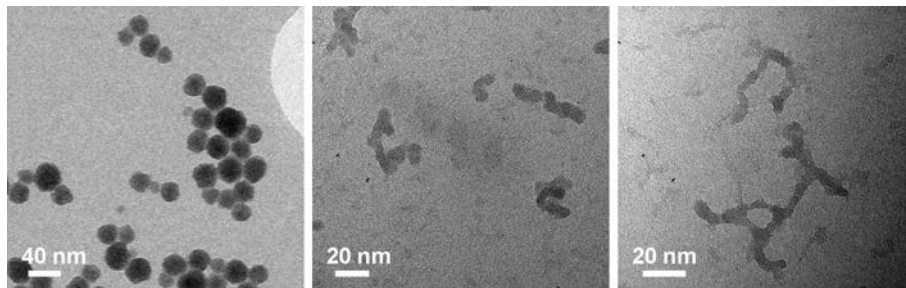


Figure 5.1: The most characteristic differences of the three particle types. From left to right: Bindzil 40/130, Bindzil 15/500 and GB3000. Bindzil 40/130 consists of spherical particles, Bindzil XP1 consists of particle multiplets and the GB3000 aggregates are branched. It can be clearly seen that all the samples are built up from silica spheres, but the aggregation and sintering process is in different stages.

The Bindzil 40/130 particles are spherical and have the dimension 22 ± 5 nm[11]. The pre-aggregated particles are branched and irregular to a larger degree than Bindzil 40/130, see figure 5.1. The particle shape is an important piece of information for understanding aggregation dynamics. The projected cross section area, the convex area and the compactness were determined, see table 5.1. The majority part of the Bindzil 15/500 primary particles have a cross section area in the approximate size range between 20 and 400 nm², but aggregates as large as 800 nm² were detected. For GB3000, the majority of the particles were in the range between 10 and 900 nm², but one particle of 6000 nm² were found. The number of analysed Bindzil 15/500 particles was 39 and the number of GB3000 particles was 60.

Table 5.1: The mean values of area, convex area and compactness of the primary particles constituting each gel (found by image analysis). The sphere diameter data of Bindzil 40/130 is from a previous study[11]. The diameter prior to the pre-aggregation of the particles were provided by AkzoNobel, PPC AB (Bindzil XP1 and GB3000).

Name	Diameter [nm]	Area [nm ²]	Convex area [nm ²]	Compactness
Bindzil 40/130	22±5	-	-	-
Bindzil XP1	5.0	230±190	300±290	0.58±0.22
GB3000	3.6	460±890	1100±1900	0.36±0.30

5.1.2 An overview of the gel samples

Figure 5.2 shows the three particle silica hydrogel samples of equivalent thickness (70 nm) on a common length scale. It is clear from this image that the samples are structurally different, especially concerning differences in pore sizes or characteristic length scale.

Overview images stitched together from several micrographs, is presented in figures 5.3-5.6. These images are considered representative for the material, and show that the gel structures are heterogeneous. In all of the mentioned images, the individual particles, as well as the larger scale heterogeneity can be distinguished. For Gel 1, significantly larger pores (or voids) than the ones seen in figure 5.3 have also been detected during the large-scale imaging, see figure 5.4. However, we have not seen any indications of large voids being interconnected. Therefore, the mass transport properties are unlikely to be affected by these few large voids. For Gel 2 (figure 5.5), it is clear that the gel is denser than Gel 1. In the stitched micrograph of Gel 3 (figure 5.6), both the smaller and the larger particles can be distinguished. We can see that the smaller particles have formed the gel, and the larger particles seem evenly distributed in the material.

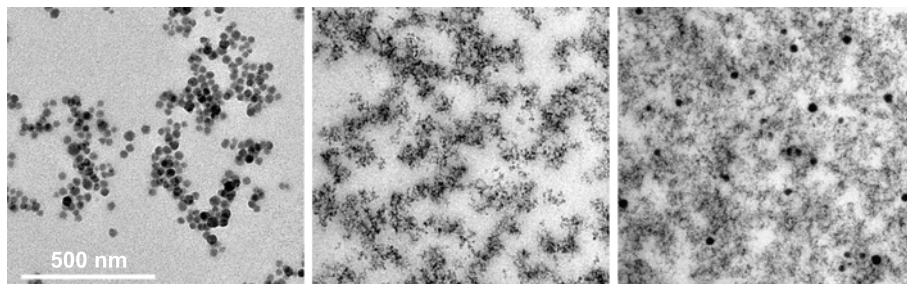


Figure 5.2: Here, the TEM images of the particulate silica hydrogel samples are presented on the same length scale (i.e. the scale bar is valid for all micrographs). The particles are perceived as darker areas in the TEM images, and the light areas are voids. These sections are all approximately 70 nm. From right to left: Gel 1, 2 and 3.

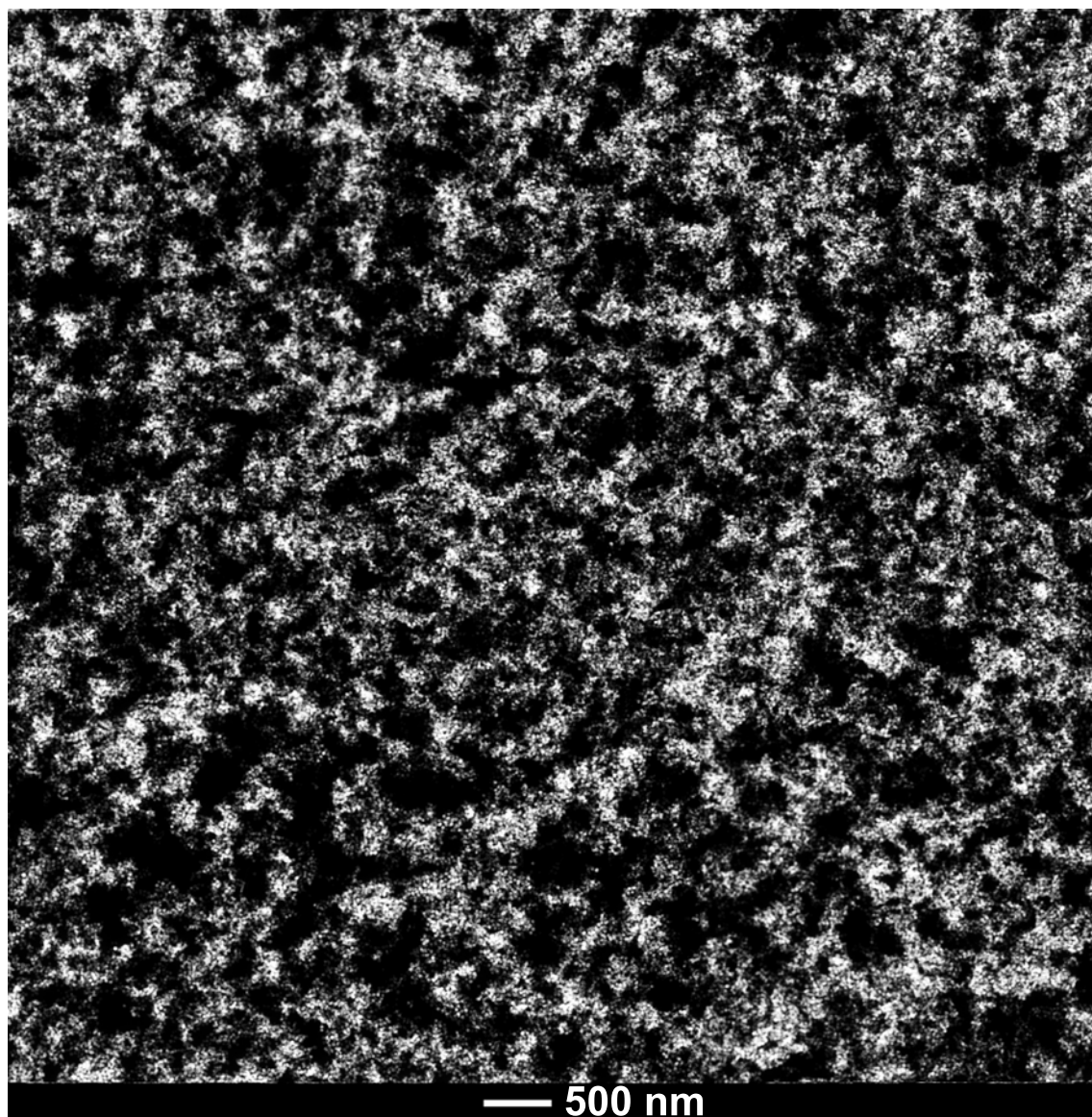


Figure 5.3: Gel 1 imaged in HAADF-STEM. The image consists of nine micrographs stitched together by post-processing.

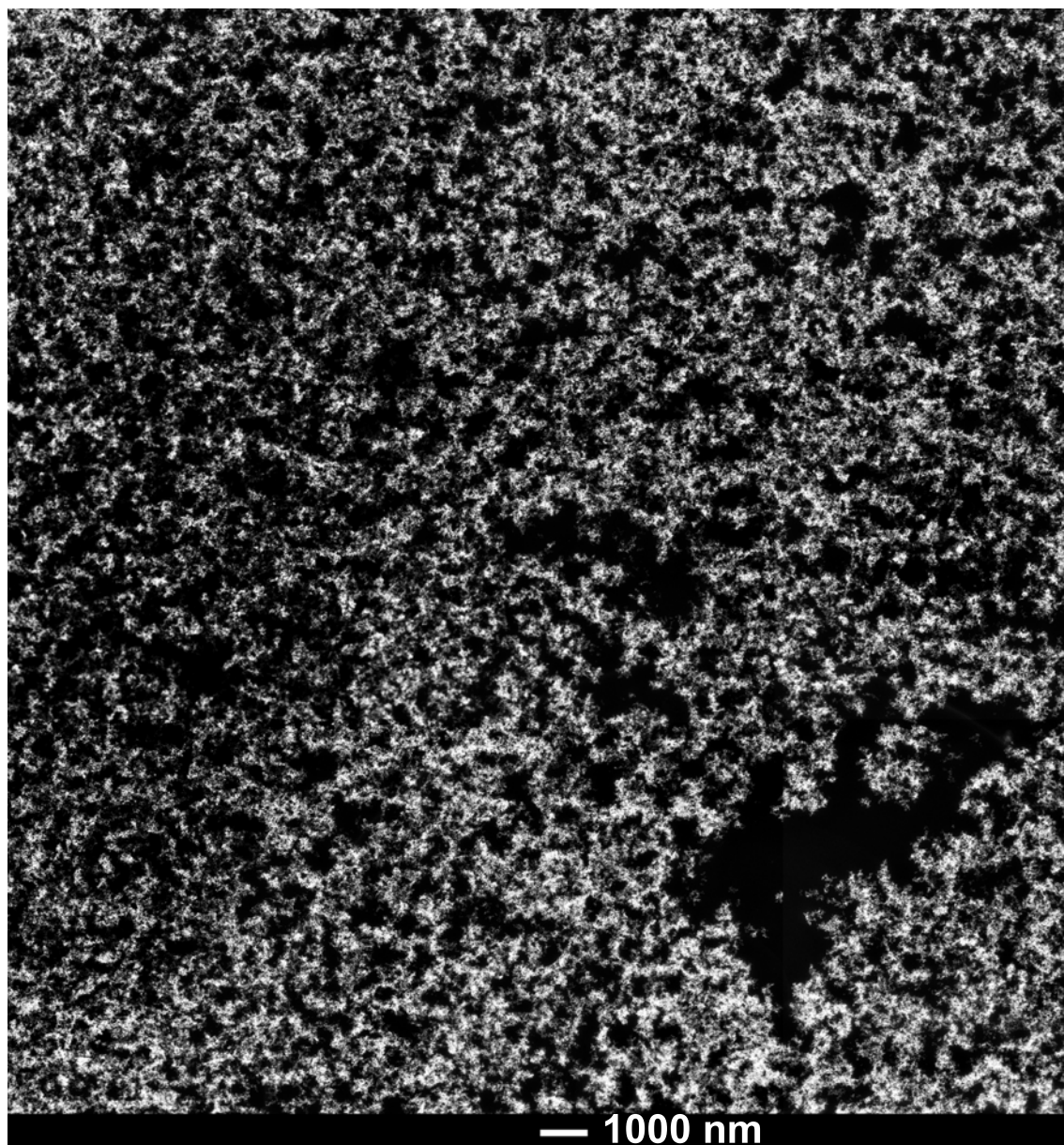


Figure 5.4: Gel 1 imaged in HAADF-STEM. The image consists of nine micrographs stitched together by post-processing. One rare large void can be seen.

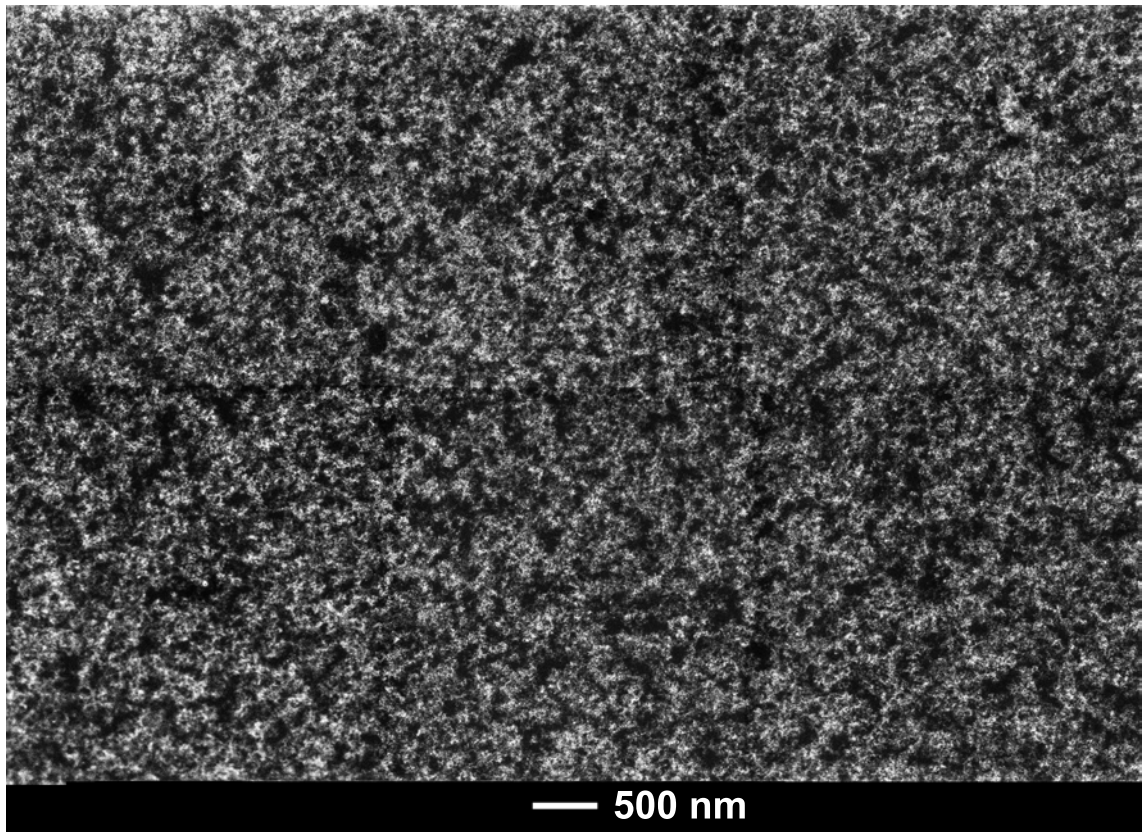


Figure 5.5: Gel 2 imaged in HAADF-STEM. The image consists of six micrographs stitched together by post-processing. This sample suffered from contamination build-up. Hence, the brightness/contrast was adjusted locally in order to reflect the imaged structure in clear way.

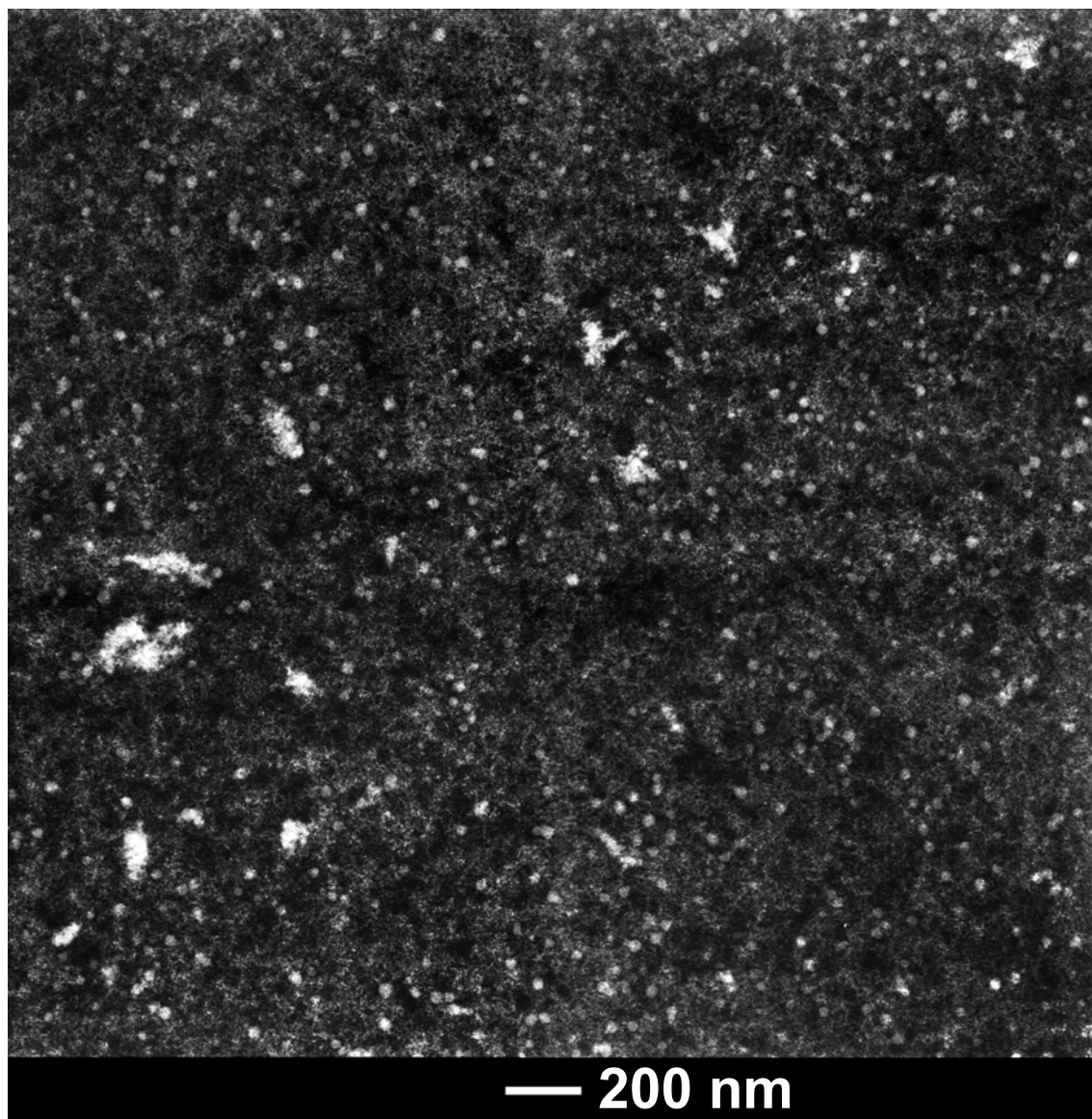


Figure 5.6: Gel 3 imaged in HAADF-STEM. The image consists of four micrographs stitched together by post-processing. This sample suffered from contamination build-up. Hence, the brightness/contrast was adjusted locally in order to reflect the imaged structure in clear way. The more intense clusters are debris on top of the sample.

5.1.3 From 2D to 3D in a STEM micrograph

Using the prior knowledge that the gel is composed of nano-spheres, the silica mass thickness could be estimated from a (two-dimensional) HAADF-STEM micrograph by means of the maximum-likelihood approach. Here, the intensity profiles of the micrographs was used as an indicator of the 3D structure. Our results provides means for direct three-dimensional quantitative structural characterisation from a STEM micrograph. Hence, it is possible to obtain a 3D reconstruction from just one 2D image. This reconstruction will, however, not be a unique solution, since several particle configurations can give rise to equal projection.

In **Paper I**, it is seen that the mass-thickness response (intensity) from the micrograph could be best fitted to the estimated power-function:

$$I(\alpha) = 0.08 + 0.64 \cdot \alpha^{0.69}, \quad (5.1)$$

where α denotes the mass thickness of silica. The numerical values in equation 5.1 denotes from left to right: the base level intensity, the curve steepness and the curve shape. This estimation provided better coherence to the micrograph intensity values, than when compared to a linear model. The 3D information in this simulated image can be used to recreate (non-unique) 3D structures corresponding to the original micrograph - an important step toward the creation of larger simulated 3D structures, and also important for statistical aggregation dynamics studies of gelation[111]. Figure 5.7 demonstrates how a reconstruction in 3D from a STEM micrograph can be presented. All isolated particles in the reconstructed 3D volume are placed at the volume boundary.

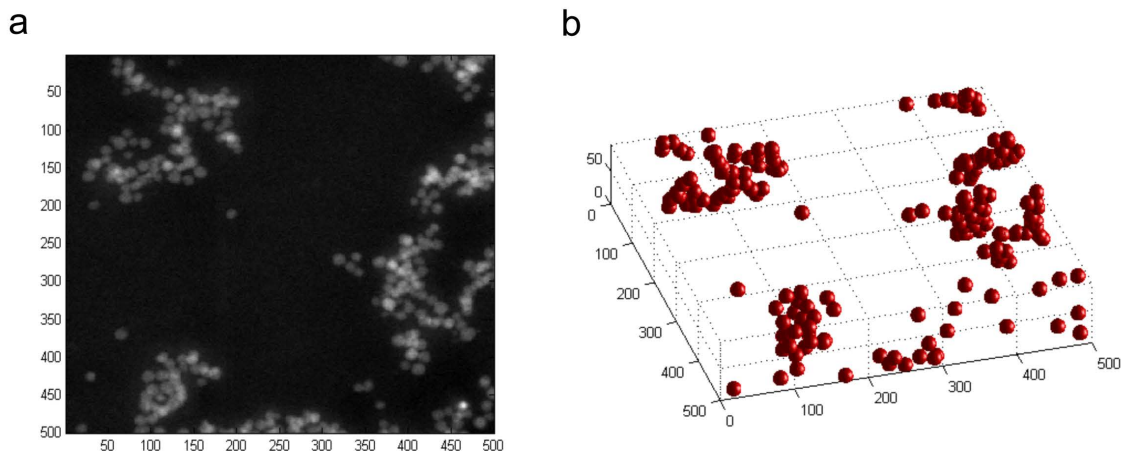


Figure 5.7: (a) A HAADF-STEM image acquired from a 90 nm thick specimen of Gel 1. (b) A simulated 3D structure from the HAADF-STEM image, constructed using intensity based mass thickness estimation. Image courtesy of Matias Nordin.

5.1.4 Electron tomography for 3D imaging

We have used ET to image the detailed three-dimensional structure of particulate silica hydrogels. One example for each of the Gels 1-3 is presented in figure 5.8. The image series for ET were recorded using HAADF-STEM.

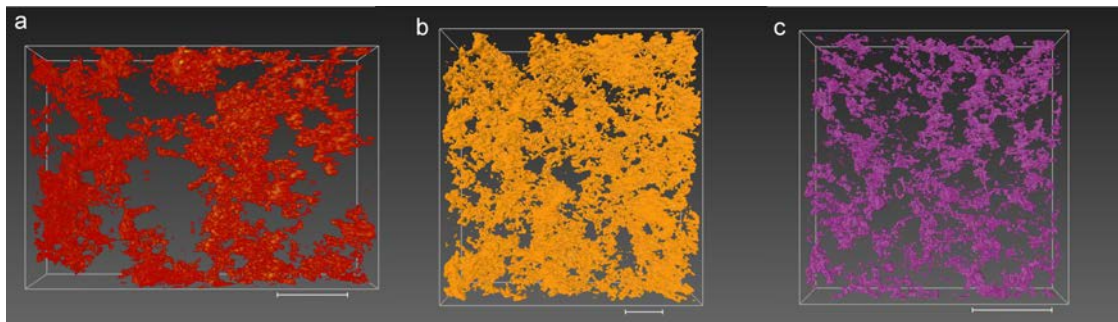


Figure 5.8: Visualisations of the tomograms of the three PSHs. Here, the binarisation is done using a global threshold which was set manually. (a) Gel 1, scale bar is 500 nm. (b) Gel 2, scale bar is 100 nm. (c) Gel 3, scale bar is 100 nm.

I have visualised the three-dimensional structure in print by presenting a set of i) the 0° micrograph from the tilt series, ii) the visualised three-dimensional tomogram and iii) the orthoslice for each corresponding plane. One example of this visualisation is shown in figure 5.9 for Gel 1 in resolution high enough to image the constituting particles and the necks between the particles to great detail. The full set of tomograms is presented in **Paper IV**.

In the visualised tomograms, the finer details of the imaged structure are sometimes lost in the reconstruction[65]. A factor contributing to the decrease in resolution is the challenges of segmentation. The complex structure of the particulate silica hydrogels would have taken an unproportional amount of time and effort to segment manually. We therefore used a global threshold for segmentation. The challenge of segmentation was recently outlined and a machine learning algorithm was proposed and demonstrated[108]. However, this is a research field on its own and is beyond the scope here.

The elongation effects and the fanning artefacts seen in almost all of the tomograms in **Paper IV** arise due to the missing wedge effect[65, 69]. Nevertheless, in figure 5.9 where the maximum tilt angle was the highest ($\pm 75^\circ$) and the number of resulting projections was the highest (90 projections), we see only minor missing wedge effects (vague streaking in the xz -orthoslice). This is in perfect agreement with literature[112]. We have also noted that the particles resemble the lemon-shape explained to be a consequence of the point-spread function[80].

The missing wedge effect in our study is a consequence of the increase in effective thickness of the thin sample section during tilt series acquisition. This makes obtaining useable micrographs from the full rotation of the sample holder impossible. Previous studies have managed to reduce the *actual* missing wedge using rod-like samples[113], dual-axis tilting[114] or full rotation tilting. Studies was also performed on reducing the *effect of* the missing wedge by different reconstruction algorithms[44, 76, 115] or by segmentation[108].

In for example Figure VI and VII in **Paper IV**, y-shaped features are present in the xz -orthoslice. This is likely a sign of sample shrinkage during tilt series acquisition. One suggested approach for decreasing this shrinkage is to pre-illuminate the sample for 3-4 minutes[79]. However, this step was not included as a standard procedure for ET here.

Some visualisations (**Paper IV**) display *arcs of intensity* (Midgley and Weyland, 2003). This is seen in Figure IX in **Paper IV** and is a sign of tilt-axis misalignment due to the micrograph alignment not fitting for the complete imaged area, which is also likely to be a consequence of beam damage. Here, as a future step, the dose could be calculated and the sample shrinkage could be quantified in order to find a low enough electron dose for imaging without this artefact. A study of handling beam sensitive materials for tomography still suggests SIRT as reconstruction mechanism for most samples, due to its robustness compared to other available techniques[116].

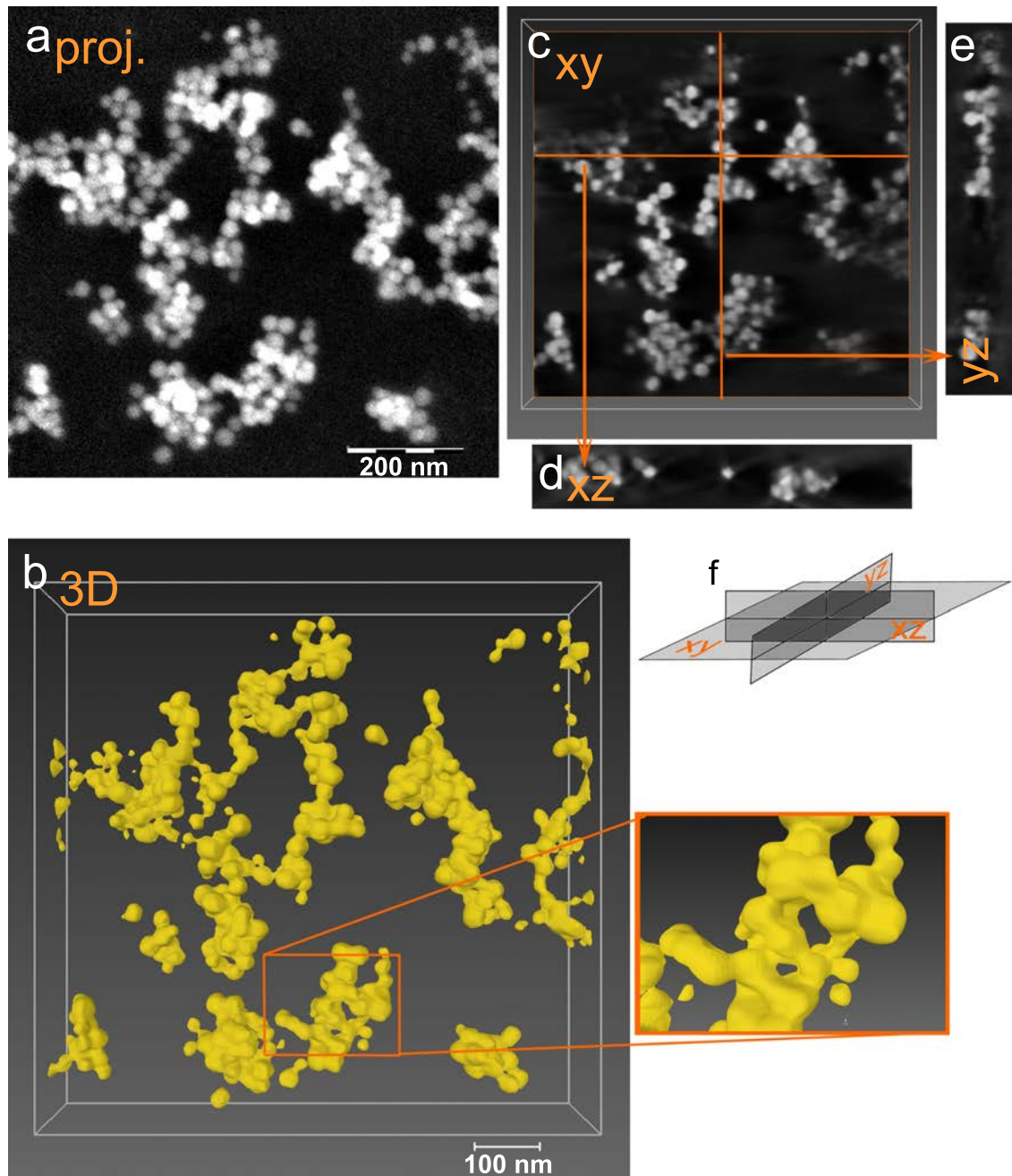


Figure 5.9: The nanostructure of the gels was revealed using ET. This figure shows an "in print"-3D-visualisation of the structure of a 70 nm thick section of Gel 1 in high resolution (80 kx magnification): (a) zero-degree-tilt STEM micrograph, (b) the tomogram visualised by volume rendering, (c-e) the orthoslices. In (f), the orthoslice configuration is illustrated. The horizontal and vertical orange lines in the xy orthoslice represent the approximate positions for the xz and yz orthoslices.

5.1.5 Fractal dimension

From each of the three PSHs, we estimated the D_f as a part of the three-dimensional sample characterisation of the silica particle network structures. The D_f estimations (computed using the box-count algorithm on the thresholded tomograms) are presented in table 5.2. The fractal dimension is estimated in a length scale range. We can see that the D_f of Gels 1 and 2 are larger than 2, meaning that they are each more fractal than a plane. Gel 3 has D_f very close to 2, hence, it is very similar in D_f as a plane. In principle, a higher fractal dimension means a denser and more crinkled structure, which relates to the aggregation mechanism for the different gels. In summary, Gels 1 and 2 are the most similar in the D_f comparison.

Table 5.2: The fractal dimension (D_f) for each of the particulate silica hydrogels. The D_f was calculated using a three-dimensional box-count method.

Sample name	D_f
Gel 1	2.11
Gel 2	2.24
Gel 3	1.97
A plane	2

These values are in good agreement with the D_f of a simulated particulate structure modelled using the Reaction Limited Cluster Aggregation (RLCA) model and having a SVF = 4.1% (as in our samples), computed equivalently.

5.1.6 Pore sizes and pore size distributions

The average pore sizes found using stereology ranged from 39 ± 6.3 nm to 530 ± 120 nm, and the geometrical average pore size ranged from 18 ± 15 nm to 310 ± 180 nm, see table 5.3. The distribution of pore sizes for each sample was attained using the geometrical pore-size-evaluation method. The 3D AMD are based on each tomogram, meaning that they do not necessarily reflect the whole sample.

Table 5.3: Structural gel parameters for the three samples. The VWMV and AMD for fitted circles were used as pore size indicators. The VWMV is presented as the diameter of an equivalent sphere, and the SE amongst the micrographs is shown. For the 2D AMD, the standard deviation amongst all individual pores is shown. The 3D AMDs are based on each tomogram.

Sample	VWMV (equivalent diameter) [nm]	2D AMD [nm]	3D AMD [nm]
Gel 1	530 ± 120	310 ± 180	177
Gel 2	120 ± 20	58 ± 32	47
Gel 3	39 ± 6.3	18 ± 15	40

The comparison between VWMV and 2D AMD is affected by the fact that VWMV does not take the thickness into account, but predicts the three-dimensional structure assuming that the image corresponds to an infinitely thin sample section[117]. The 2D AMD decreases as the thickness increases. It is also area-weighted, by definition. The 3D AMD is volume-weighted.

In figure 5.10, the AMD found in **Paper II** and **Paper V** is shown. We can clearly see that the 3D values differ from the values based on a set of 2D images, and that Gel 2 and 3 are more similar than anticipated from the two-dimensional micrographs. One reason for this might be that more particles can fit in the z-direction, and since they are branched, this could create the illusion of a

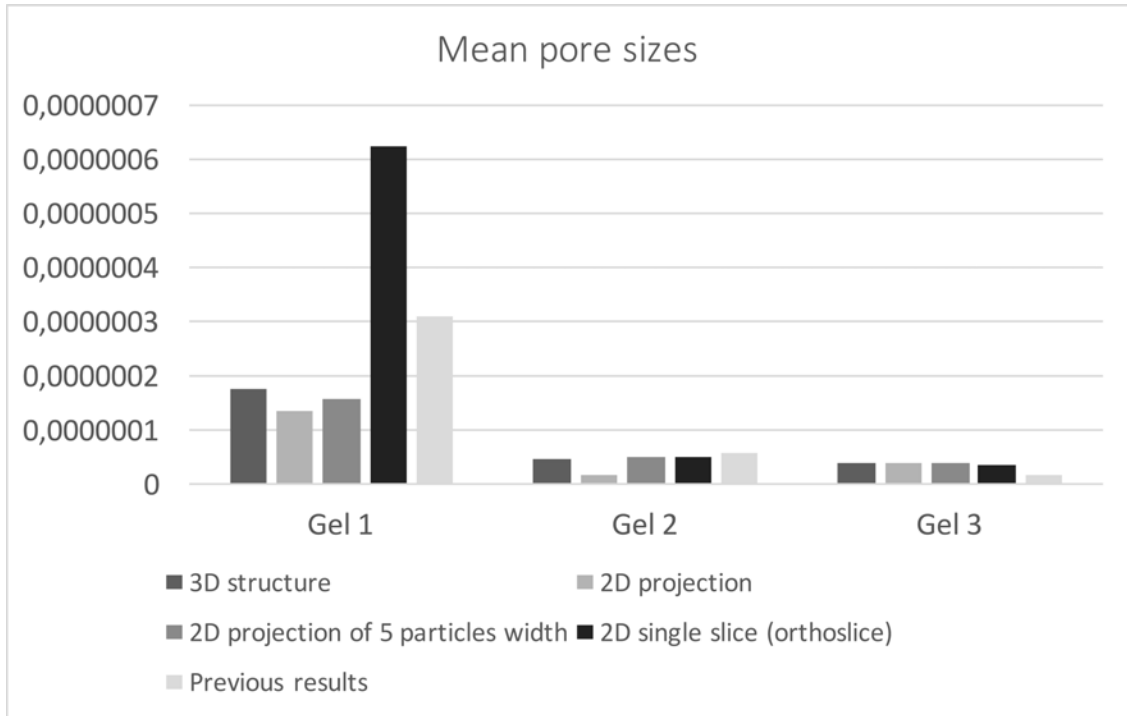


Figure 5.10: A comparison of the AMD from the 3D structure (tomogram), the 2D projection (projected from the binary tomogram), the 2D projection of five particle width (also projected from the binary tomogram), and the results from the two-dimensional set of images presented in **Paper II** (previous).

much more dense gel. There is however no doubt that Gel 3 have smaller pores than Gel 2, based on the visual inspection described in the Experimental section. Other reasons for the similarities of the 3D AMD might be from the loss of fine structures in the tomogram, or from the difference in number of sampled pores in the 2D study compared to in the 3D study.

5.1.7 Interconnectivity and accessible pore volume fraction as a function of probe size

The interconnectivity and accessible pore volume fraction of the porous channels, cannot unambiguously be obtained from the two-dimensional data. However, we have compared the interconnectivity and accessible pore volume fraction of the particulate silica hydrogels quantitatively, as a function of probe size (i.e. the size of an imaginary object transport in the structure). The accessible pore volume fraction and interconnectivity for Gels 1-3 is presented in figure 5.11.

From the accessible pore volume fraction quantification, we see that Gel 1 allows a probe of approximately 160 nm access to 50% of the pore network. For Gel 2, the equivalent is valid for a probe of approximately 50 nm. The results indicate that Gel 3 is less interconnected than Gel 2 when the probe size exceeds approximately 30 nm. This difference between Gel 2 and Gel 3 is smaller than expected from the pore size distribution analysis performed on two-dimensional images in **Paper II**. However, this result could be part of the explanation for the very similar values measured for mass transport in **Paper II**.

We can see that the interconnectivity of Gel 1 is equal to 1 up to approximately 120 nm, while Gel 2 and 3 have a shorter maximum span. A rapid decrease in interconnectivity as a function of probe size can depend on a high degree of pore throats in the sample. Hence, the large and sudden

drops in interconnectivity seen for Gel 2 and 3 indicate the presence of prominent narrow

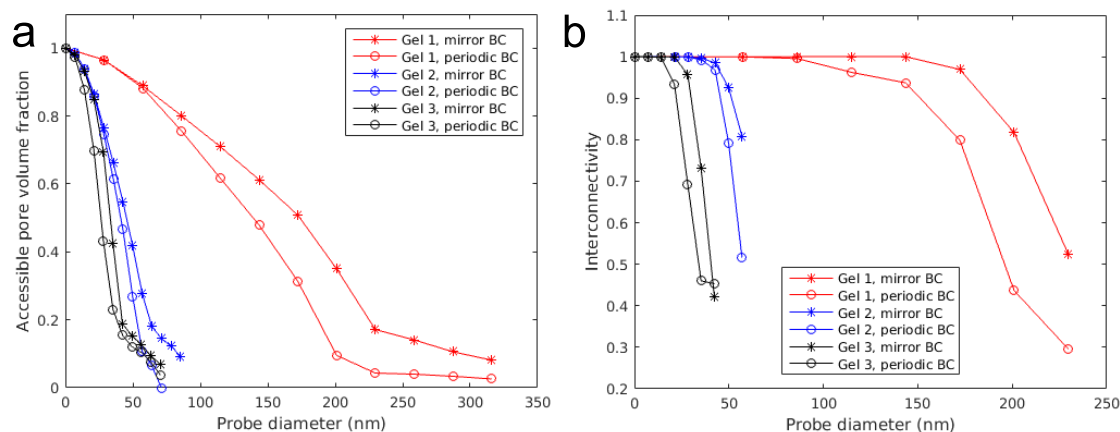


Figure 5.11: (a) The accessible pore volume fraction of all gels plotted as a function of probe diameter. (b) The interconnectivity of the pore volume of all gels plotted as a function of probe diameter. The data points are joined by lines for guiding the eye. Image courtesy of T. Gebäck.

connections within the pore volume, or at the periodic or mirrored boundaries.

Comparing the accessible pore volume fractions with the 2D mean pore diameter from figure 5.10 and table 5.3, we see that Gel 3 differentiates from the other two concerning how the accessible pore volume fraction correspond with the mean pore size. For Gels 1 and 2, a probe with a size equivalent to the mean pore size of the gel experience an accessible pore volume fraction of approximately 10-20%. For Gel 3, the equivalent comparison gives an accessible pore volume fraction of over 90%. However, when reviewing the AMD in 3D for the tomograms, a probe of the mean diameter size of Gel 1 will instead have access to 40% of the pore volume, for Gel 2 it would have access to 50% and for Gel 3 the equivalent would be 20%.

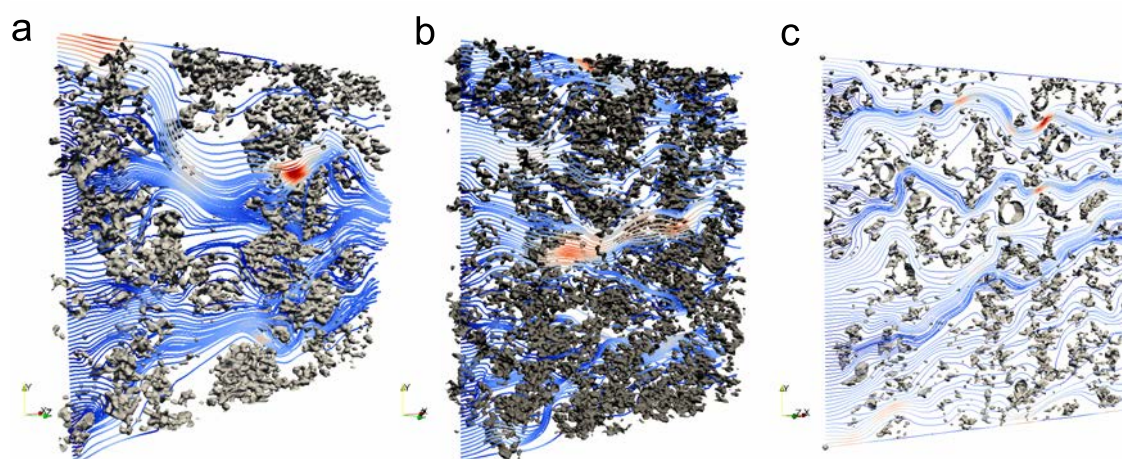


Figure 5.12: The segmentation resulted in these geometries, used for flow and diffusion simulations. (a) Gel 1, (b) Gel 2, (c) Gel 3. The color scale is relative and light blue is the lowest flow rate while red is the highest. There are a certain evenly distributed flow lines entering the structure. As they proceed into the structure, the distances between them will change as a direct function of the structure. Image courtesy of T. Gebäck.

Table 5.4: Gel parameters for mass transport data for the three samples. The SE values of the flow speed (FS) were calculated with linear regression approximation. For the diffusion coefficients (D), the SE is obtained from a Monte Carlo estimate of the variance in the raw NMR diffusion data. The Re is presented to the order of 10^{-8} . In this setup, only Gel 1 is approximately close to a situation where flow and diffusion have similar impact, as concluded from the Pe.

Sample	FS [mm/day]	D [10^9 m ² /s]	Re	Pe
Gel 1	2.5±0.091	2.04±0.02	0.9	0.74
Gel 2	0.59±0.043	1.99±0.02	0.04	0.10
Gel 3	0.58±0.039	1.98±0.02	0.01	0.10

5.2 Structure vs. fluid transport properties in particulate silica hydrogels

For Gel 1, the majority of the pores are larger than 100 nm with the largest detected pores around 1000 nm. Based on this data, Gel 1 is expected to be permeable to water in a pressure driven flow[15], even at very moderate pressure differences. In Gel 2, a minority of the pores are larger than 100 nm, and the largest detected pore is approximately 180 nm. Although the histogram tail represented by large pores is small, it may have a significant impact on the permeability of the gel. It should however be noted that in order to quantify the effect of the tail on the flow rate with certainty, three-dimensional microstructure data, containing information about e.g. connectivity, would be needed. For Gel 3, all pores were smaller than 100 nm. If a small pressure difference drives the flow, diffusion is likely to dominate the mechanism for transporting the liquid. Practically no liquid was therefore expected to penetrate the gel plug in the pressure driven flow measurements of Gel 3[15]. However, there were slow but clearly detectable flows also through the two gels with the smallest pores

The self-diffusion constant D_0 for liquid water in the particulate silica hydrogels was studied by NMR diffusometry. The self diffusion constants and the flow rate values are presented together with the Reynolds and Péclet numbers are presented in table 5.4. The mass transport in all three samples were according to their Péclet (Pe) numbers dominated by diffusion. However, the contribution from convective flow on the total transport was also according to the Pe number much greater for Gel 1 than for the other two gels. Gel 2 and 3 had almost identical convective flow rate data, despite a clear structural difference.

The higher magnification tomograms were used as templates for *in situ* simulations of the convective flow, using LBM (see figure 5.12). As in the determination of the interconnectivity and accessible pore volume fraction, the tomograms were stacked either periodically or by mirroring for the LBM of the mass transport. The differences between the simulated and measured permeabilities are very large, see table 5.5 and figure 5.13.

Table 5.5: A comparison between the permeabilities from measured and *in-situ* simulated data. For the simulated values, the lower value represent the periodic boundary condition and the higher value represents the mirror boundary condition.

Sample name	Permeability from measurements	Simulated permeability
Gel 1	$1.2 \cdot 10^{-15}$ m ²	$0.65 - 0.72 \cdot 10^{-15}$ m ²
Gel 2	$1.4 \cdot 10^{-16}$ m ²	$1.2 - 1.3 \cdot 10^{-15}$ m ²
Gel 3	$1.4 \cdot 10^{-16}$ m ²	$1.2 \cdot 10^{-15}$ m ²

One challenging aspect of using the tomograms as virtual simulation templates was their limited

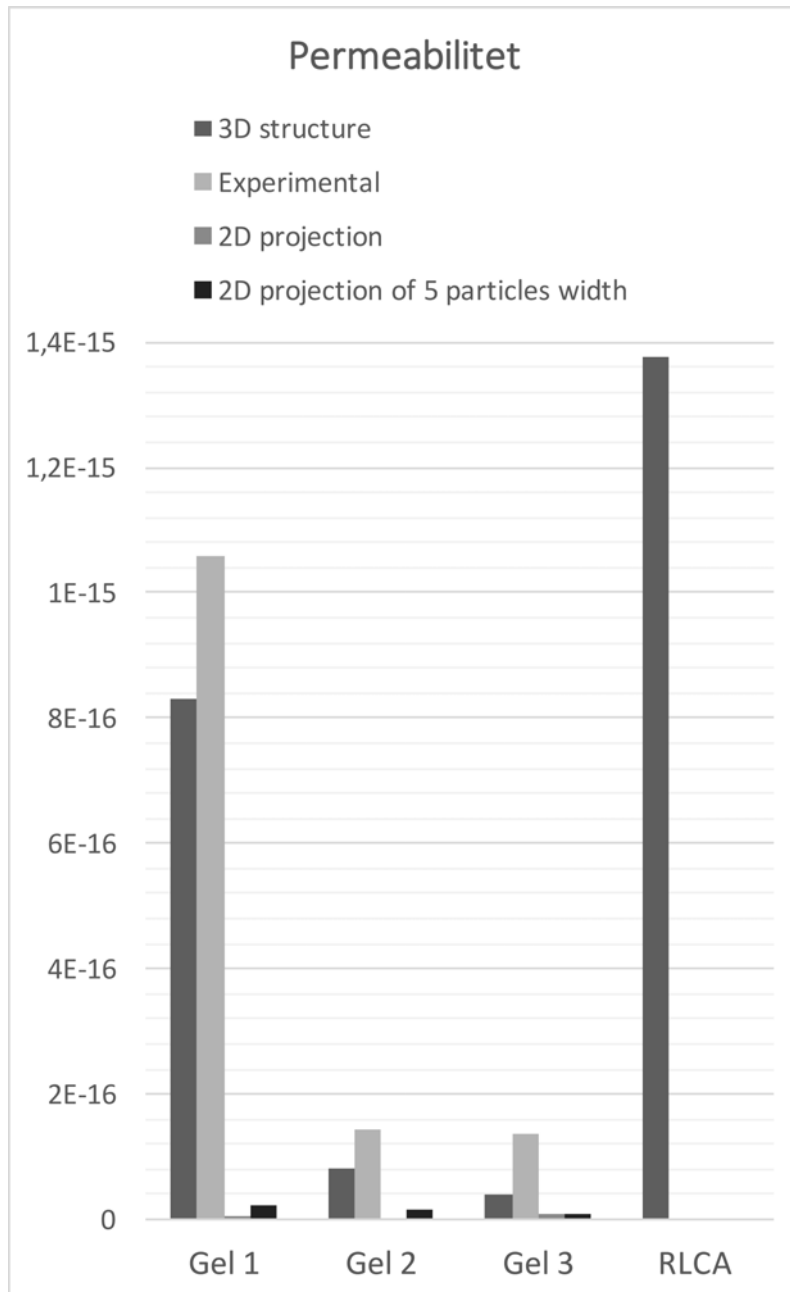


Figure 5.13: The permeabilities for the PSH samples from the LBM simulations in the tomograms (3D structure), the experimental data measurements (Experimental), the projected tomogram (2D projection) and a thin projection of 5 particle diameters thickness (2D projections of 5 particles width).

thickness. Ideally, the thickness should represent the representative volume, and more. Yet, finding out the representative volume for an sample template is a task which requires strategy. Here, by performing LBM flow simulations in slices of different thicknesses of a computer simulated structure equivalent to Gel 1, we took a step towards finding out the representative volume, but most importantly, this knowledge can help us explain the simulations, which does not directly conform with the flow rates measured experimentally. This LBM of the flow rate in a RLCA-modelled structure equivalent as closely as possible to Gel 1 is shown in figure 5.14. As the thickness of the section in which the LBM takes place increases, the values for the mirrored and the periodically stacked templates seem to converge. The corresponding experimental and simulated flow rate values are also included in figure 5.14.

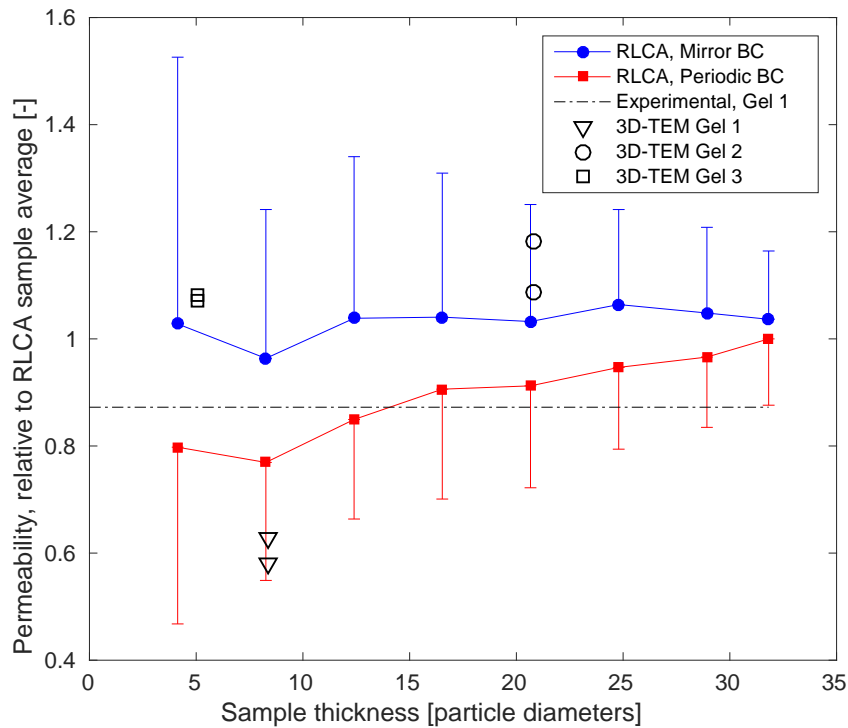


Figure 5.14: A comparison between the permeability of increasingly thicker sections of a simulated particulate structure, created by RLCA modelling with an aggregation probability of $p=0.0001$. The structures were extended either by mirroring or by parallel stacking, as previously performed for interconnectivity quantification in the PSHs **Paper IV**. Included is also the experimental permeability values for the Gel 1, which happen to fit the permeability for the RLCA structure well. The permeability values for each of Gel 1-3 are included in the graph, the span being between the mirrored and the parallel stacking approach. Also, the average pore sizes for 2D and 3D measurements are shown for Gel 1. In this plot we can see how the accuracy of the permeability increases with sample thickness. The permeability results for mirrored and periodic boundary conditions are converging towards a representative sample volume for LBM. We can also clearly see that Gel 2 is definitely in the region of representative volume. Hence, we expect the simulated permeability values for Gel 2 to be the best corresponding to the experimental data. Image courtesy of T. Gebäck.

5.3 Aggregation dynamics during gelation of particulate silica hydrogels

The gel structure was simulated using different cluster aggregation probabilities, p : DLCA ($p = 1$) and RLCA ($p \in \{0.1, 0.01, 0.001, 0.0001\}$). Slices with a thickness of 90 nm from these simulated gels were extracted and transformed to a projection and subjected to noise, making them as similar to experimental STEM micrographs as possible. These simulated micrographs and the experimental micrographs were investigated using different summary functions from spatial statistics (the empty space function F , Ripley's K -function L , the clustering function c , and the mean cluster size function M) for summarising and quantifying their similarities and differences.

We concluded that according to the summary functions, the probability of aggregation which creates the simulated gel sample to resemble the experimental micrographs the most was $p = 0.0001$, i.e. the lowest p . However, the clustering function c , indicates that $p = 0.1$ seems to model the short-range repulsive behaviour within a cluster best.

The results show that information of structure aggregation dynamics *can* be concluded by using merely two-dimensional STEM images, without having to image gel samples at different stages in the gelation process. This finding can significantly increase the accessibility to aggregation dynamics data of particulate gel structures.

Since the link between experimental observations and the theory describing the underlying mechanics for gel formation is incomplete, the 3D tomograms of the gels will be used to study particle aggregation also in 3D for particulate silica hydrogels. The tomograms of particulate silica hydrogels imaged using ET have already been compared with simulated aggregated structures. We again used a summary tool from spatial statistics, the L -function, for the comparison between experimental and simulated data. These preliminary results were evaluated within the DLCA/RLCA modelling framework, see figure 5.15. The three-dimensional aspect of the study provides results more coherent with DLCA/RLCA theory than presented in the two-dimensional study in paper **Paper III**.

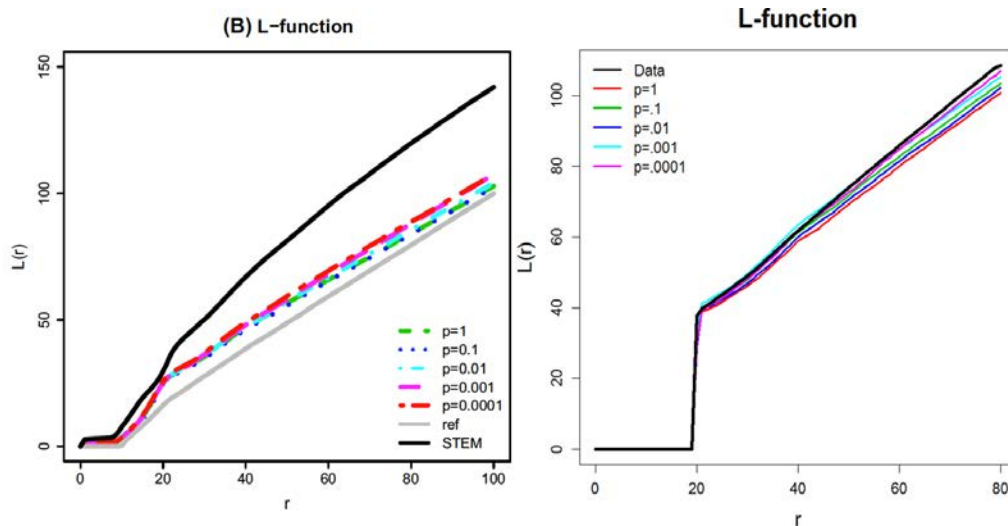


Figure 5.15: On the left, the two-dimensional data is summarised using the L -function. Here, the STEM data and the closest RLCA curve is still far from each other. However, in the equivalent 3D study (right curve), the L -function of the RLCA model with $p = 0.0001$ is significantly closer. The 3D information is, hence, absolutely crucial for aggregation model evaluation. Image courtesy of H. Häbel.

5.4 Experimental considerations for ET on PSHs

In order to perform ET of high quality on particulate silica hydrogels, there are a few things in the sample preparation, image acquisition and visualisation which have proven to be extra important during my work. There are numerous articles and some books which go in depth on the subject of ET, yet, starting from scratch, there are a few key strategies and practical details that in my experience are advantageous to know about early on in the process. These things are briefly described in this section in order of appearance during the experimental process. This section presumes that the reader has some basic knowledge about electron microscopy. I recommend *Transmission electron microscopy : a textbook for materials science*[63] with the recently added chapter *Transmission Electron Microscopy*[69].

Embedding

The thin sectioning of the finer gel samples proved challenging due to the lack of contrast between the sample and the surrounding plastic. I found that dusting the plasticised gel cubes with talcum powder prior to embedding the cube a plastic block provided the contrast necessary to localise the cube within the plastic block.

Avoiding beam blockage by the grid

During the acquisition of a tilt series, there is always the risk that the region of interest will become blocked by a bar of the sample support grid. One beneficial precaution against this is to already when positioning the sample in the TEM holder is to orient the sample so that the grid bars form a 45° angle with the tilt axis which is parallel to the length of the holder. This ensures that as much as possible of the sample can be seen during tilting. To avoiding beam blockage is also important for the reduction of the missing wedge. Using a coarser grid would make finding suitable positions for tomographic investigations easier, but it might not provide the mechanical support needed.

Pre-conditioning or not?

In literature, pre-conditioning (illuminating a large area of the sample) is sometimes recommended for plasticised sections for reducing contamination buildup on the sample or reducing shrinkage of the sample during the tilt series acquisition[79]. However, I did not experience any clear benefits from a pre-conditioning procedure during my work.

STEM vs. TEM imaging

During my work, we performed a direct comparison of ET using either TEM or STEM. The resulting tilt series and tomograms showed that STEM provided better signal-to-noise ratio, higher contrast and better focus. It also enables dynamic focus, meaning that the focused electron beam which scans the sample during STEM imaging will be focused for ideally all points in the sample during the tilt series acquisition. The selection of STEM over TEM is also generally recommended for material science[67, 69].

HAADF detector adjustments

In order to get the best images, the full potential of the detector should be used. This is achieved by iteratively changing the brightness and contrast settings for the *Scope* option. The option provides a graph displaying the intensity values along for example a line in the image. By iteratively changing the brightness and contrast settings, the graph should be adjusted to display as large differences in intensity as possible between the background and the brightest areas, without saturating the detector.

Camera length

The camera length (meaning the effective distance from the sample to the detector) needed to be

adjusted in order to get the maximum contrast between the plastic and the silica. This can be done before every tilt series acquisition by acquiring an image sequence while only changing the camera length. The camera length giving an image of highest contrast should be used for the rest of the micrographs during the session. This strategy was also used in a recent study[118].

Dwell time

The time period that the electron beam lingers at each point during the sample is decided by the *dwell time*. A high dwell time gives an image of higher resolution and better signal-to-noise ratio. However, a higher dwell time significantly increases the time for the tilt series acquisition.

Selecting tilt angles and increments for sectioned samples

We used the Saxton scheme[71] as previously described in section 2.4. Hence, a greater number of micrographs per angle is acquired for higher tilt angles. Acquiring a tilt series for $\pm 75^\circ$ instead of $\pm 70^\circ$ adds 11 images to the tilt series if the angular increment at 0° is 2.5° . Also, changing the angular increment from 3.0° to 2.5° at 0° , increases a tilt series of $\pm 70^\circ$ with 12 images. In my experience, this increase in image numbers made a huge difference for reducing the missing wedge effect on the reconstruction. The beneficial effect of higher tilt angles is also well known according to literature[112]. However, the benefits of decreased angular increments have recently been subject to dispute for beam sensitive materials[112]. Adding more images to the series of course makes the total acquisition time longer and electron beam dose higher.

Focus

The autofocus functions of the acquisition software for ET work differently well on different samples. Hence, all my tilt series were focused manually. Well focused micrographs are crucial for the ET result and for the image alignment[108]. However, if the sample contaminates a lot (as my particular samples did) the scanning of the STEM sometimes leave light areas with sharp edges on the sample surface, especially during fine tuning of the focus while using the smaller focus window. Therefore, its beneficial to focus the images while looking directly at the whole region of interest. As the software (Xplore3D by FEI) awaits the user to adjust and confirm the focus, the dynamic focus will be turned of. Hence, if the top and bottom part of the image on the screen is *symmetrically* out of focus while the sample is at a tilt angle, the sample is in proper focus!

Alignment

The alignment is performed using cross-correlation, and the user needs to adjust the image filtering for supporting the cross-correlation algorithm, which is repeatedly applied to the image until a high enough precision in the alignment is reached. For an even better alignment, an additional adjustment of the filters can be beneficial even after a few repetitions of the cross-correlation. The importance of image alignment and tilt axis adjustment cannot be stressed enough[69, 108]. If the alignment in one software fails, it can help to try another software, for example IMOD[96].

Visualisation

If the tomograms are noisy, 3D filters for removing noise is available in Avizo 8.1. I used the edge-preserving smoothing in the xy-plane and a Gaussian 3D-filter on Gel 2 in high magnification.

Also, there is a fine balance between keeping too much features arising from the missing-wedge and removing too much of the finest structure in the sample. This is a motivation for further explore the techniques for circumventing the missing wedge.

Chapter 6

Summary of included papers

In this section, the topic of investigation, the results, the importance, and the connection between the papers are summarised for each of the included papers. Figure 6.1 illustrates how the included papers are connected. Due to the intertwined character of these connections, the articles are presented in chronological order.

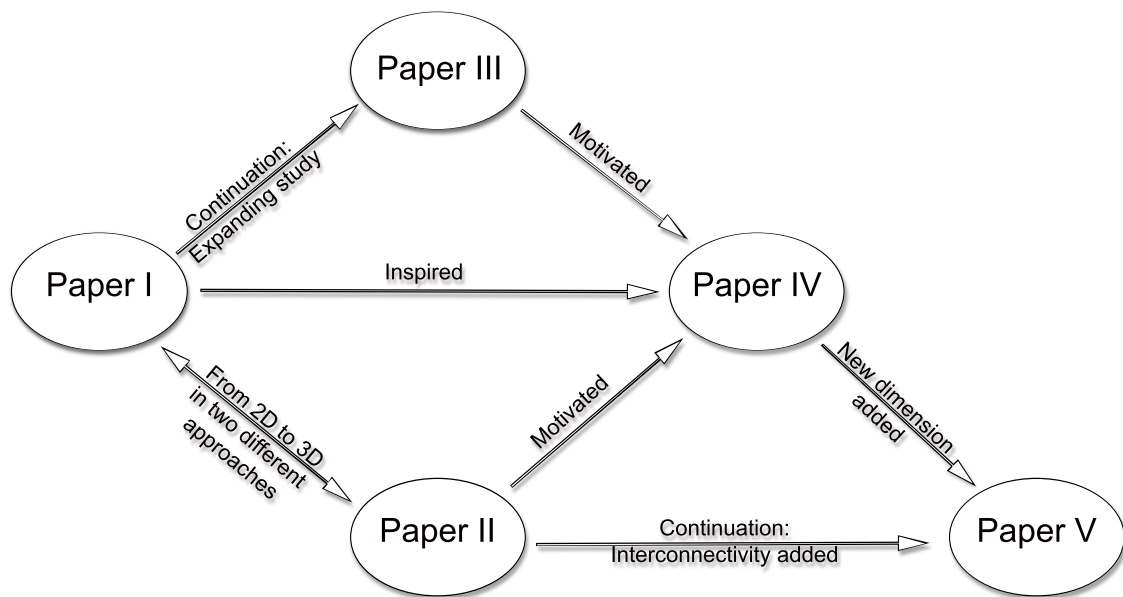


Figure 6.1: This figure shows how the included papers are connected. Due to the intertwined character of the connections, the articles are presented in chronological order.

6.1 Paper I

This paper evaluates a mass thickness-response estimation from a HAADF-STEM micrograph of an embedded particulate silica hydrogel sample of 9.0 weight percent¹. The silica mass thickness was estimated from the micrograph, using the prior knowledge that the gel is composed of nanospheres. Using a statistical maximum likelihood approach for addressing the challenge of making deductions of the third dimension from 2D micrographs, the intensity profiles of the micrographs was used as an indicator of the 3D structure.

We showed that the intensity I , which is the detected output from the micrograph mass thickness², Z , could be best fitted to the estimated power-function

$$I(\alpha) = 0.08 + 0.64 \cdot \alpha^{0.69}, \quad (6.1)$$

where α denotes the mass thickness of silica. This estimation provided better coherence to the micrograph intensity values, than when compared to a linear model evaluated using a Chi-squared test.

Every STEM micrographs are naturally not compliant with the demonstrated function. However, the maximum likelihood approach can be used for estimating an intensity relationship to STEM micrographs when some information of the underlying geometry or topological features are known. Our results provides means for direct three-dimensional quantitative structural characterisation from a STEM micrograph. Hence, it is possible to obtain a 3D reconstruction from just one 2D image. This reconstruction will, however, not be a unique solution, but is still valuable for e.g. statistical gel aggregation studies and for creating larger 3D structures to be used in validation with computer simulations of e.g. convective flow or diffusion. The paper provides fundamental understanding of why actual 3D imaging is important, especially as a validation step for more statistical methods by which larger structures can be simulated.

This study was continued and expanded in the study of aggregation dynamics of silica particle clusters from two-dimensional micrographs, presented in **Paper III**. This paper also served as inspiration for determining the unique sample structure using ET, as demonstrated in **Paper IV**. The 9.0 weight percent particulate silica hydrogel sample was (inexclusively) used in all included papers, and is denoted "Gel 1" in **Paper II**, **Paper IV** and **Paper V**.

6.2 Paper II

In this study, we address the correlation between nanoscale pore structure and water transport properties from a two-dimensional perspective. We identified how the mean pore sizes correlated with the measured water transport through three different particulate silica hydrogel samples. The pore sizes of the samples were on different length scales, but they had equal weight percentage of silica. The gel samples were characterised concerning their pore sizes, pore size distribution, intrinsic surface area and the morphology of the particles constituting them. The mean pore sizes were determined by using a stereological and a geometrical ("circle-fitting") evaluation method. The mass transport properties of the samples were tested using gravitationally driven steady state flow and NMR diffusometry. The structural characterisation of the gels was performed by analysing 2D ET micrographs.

The average stereologically determined pore sizes ranged from 39 ± 6.3 nm to 530 ± 120 nm, and the geometrically determined pore sizes ranged from 18 ± 15 nm to 310 ± 180 nm. The distribution of pore sizes for each sample was attained using the geometrical pore-size-evaluation method. Our results experimentally verified the existence of a non-linear relationship between pore size and flow speed at the investigated length scales. The coarser gel ("Gel 1") was separated from the other two ("Gel 2" and "Gel 3") by a factor of 4.3 in flow speed. Gel 2 and Gel 3 presented almost

¹9.0 wt% is the correct value, see errata list.

² $I \propto Z^{1.7}$ [119]

identical flow speed data, although, their stereologically measured pore sizes differed with a factor between 2.2 and 4.3. The mass transport in all the samples were diffusion dominated according to their Péclet (Pe) numbers. However, the contribution from convective flow on the total transport was also according to the Pe number much greater for Gel 1 than for the other two gels.

The article provides new insight in mass transport on the nanoscale: two of the three investigated samples had near identical convective flow data, despite a clear structural difference. Our results on where either diffusion or convective flow is the dominating liquid transport mechanism showed relevant for research in diverse fields from basic diffusion science[120] to biotechnology[121].

The apparent contradiction between flow speed and pore structure needed to be investigated further, which motivated determining the three-dimensional structure (presented in **Paper IV**) for the 3D analysis of the pore volume as presented in **Paper V**, where the experimentally acquired 3D structures also served as mass-transport simulation templates. The three different particulate silica hydrogels are denoted "Gel 1", "Gel 2" and "Gel 3" also in **Paper IV** and **Paper V**.

6.3 Paper III

In this paper, we performed a quantitative comparison of ET micrographs to simulated micrographs for evaluating the aggregation dynamics during gel formation. Several simulated aggregation scenarios with different cluster aggregation probabilities were compared, and the experimental ET micrographs served as a key for evaluating the aggregation dynamics simulation.

In the physical world, the network structure of a particulate silica hydrogel is formed as a function of different unknown probabilities for aggregation. For understanding and modelling the aggregation process within the sample, the Diffusion Limited Cluster Aggregation model (DLCA) or the Reaction Limited Cluster Aggregation model (RLCA) can be used. The RLCA model includes repulsive forces, but the DLCA model does not. The smaller the probability of cluster aggregation, the more prominent is the RLCA aspect of the aggregation dynamics.

The gel structure was simulated using different cluster aggregation probabilities, p : DLCA ($p = 1$) and RLCA ($p \in \{0.1, 0.01, 0.001, 0.0001\}$). Slices with a thickness of 90 nm from these simulated gels were extracted and transformed to a projection which was subjected to noise, making it as similar to an experimental ET micrograph as possible. The simulated micrographs and the experimental micrographs were investigated, using four different summary functions from spatial statistics (the empty space function F , the "L-function" L , the clustering function c , and the mean cluster size function M) for capturing their similarities and differences.

We concluded that according to the F , L and M functions, the probability of aggregation which creates the simulated gel sample that resembles the experimental micrographs the most was ($p = 0.0001$). However, the clustering function c , indicates that $p = 0.1$ seems to model the short-range repulsive behaviour within a cluster best.

This paper shows that information of structure aggregation dynamics can indeed be concluded by using merely two-dimensional ET images, without having to image gel samples at different stages in the gelation process: A finding that significantly can increase the accessibility to three-dimensional analysis of samples where prior knowledge of sample geometry is available. The method presented in **Paper I** is used for determining the particle positions here. A similar study including three-dimensional experimental data is a subject for future investigation, and preliminary data is included in the *Summary of results and discussion* section.

6.4 Paper IV

This paper is dedicated to the challenge of revealing the detailed three-dimensional nanoscale pore structure and connectivity of a soft porous material in three dimensions. We have used ET to image the detailed three-dimensional structure of particulate silica hydrogels. A full understanding of the transport properties of these gels requires knowledge about the pore structure and in particular

the interconnectivity in three dimensions, since the transport takes the path of lowest resistance. The image series for ET were recorded using HAADF-STEM. The interconnectivity and accessible pore volume fraction of the porous channels were obtained from the three-dimensional tomography studies since it cannot unambiguously be obtained from the two-dimensional data. We make a quantitative comparison of interconnectivity and accessible pore volume as a function of size of mass-transport object in the three different hydrogels based on direct images on the nanoscale.

We have, for the first time, revealed the structure of particulate silica hydrogels with mean pore sizes less than 500 nm, using ET. From the tomograms, we quantified the interconnectivity and accessible pore volume fraction of the three samples. The pore interconnectivity of a porous material has not earlier been studied on the nanoscale using methods taking the 3D unique structure and morphology of the pores into account. There is a critical thickness for each sample determined by its scattering properties (e.g. by the volume fraction of silica), sample section thickness and the contrast mechanism used for ET imaging, which we have handled the challenge of critical thickness by extending the tomograms to larger volumes by either mirroring the structure or stacking them periodically.

From the accessible pore volume fraction quantification, we see that Gel 1 allows a probe of approximately 160 nm access to 50% of the pore network. For Gel 2, the equivalent goes for a probe of approximately 50 nm. The results indicate that Gel 3 is less interconnected than Gel 2 when the probe size exceeds approximately 30 nm. This difference between Gel 2 and Gel 3 is smaller than expected from the pore size distribution analysis performed on two-dimensional images in **Paper II**.

The interconnectivity provides information on to what extent the pore network is connected on a specific length scale. A connectivity that maintains a maximum level longer indicates that the pore volume is well connected for even larger probes. We can see that the interconnectivity of Gel 1 is equal to 1 up to approximately 120 nm, while Gel 2 and 3 have a shorter maximum span. A rapid decrease in interconnectivity as a function of probe size can depend on a high degree of pore throats in the sample. Hence, the large and sudden drops in interconnectivity seen for Gel 2 and 3 indicate the presence of prominent narrow connections within the pore volume, or at the periodic or mirrored boundaries.

Three-dimensional material information is important for understanding the connection between material structure and material properties. Our presented use of ET imaging and subsequent interconnectivity quantification of particulate hydrogels demonstrate the possibilities for imaging porous soft materials (from bulk or membranes) in three dimensions, on the nanoscale. It also enables an additional dimension in statistical gelation studies (aggregation dynamics). Hence, we suggest applications within mass transport studies on the nanoscale, as well as within aggregation dynamics.

This paper has strong connections to all included papers.

- In **Paper I**, we demonstrated an approach for determining a corresponding three-dimensional structure from HAADF-STEM micrographs. Motivated by this, we here demonstrate a way to also reveal the unique and local material configuration, using ET.
- It answers to the need for the three-dimensional structure requested in **Paper III**, enabling the three-dimensional evaluation of different aggregation dynamics models presented in **Paper VI**.
- In **Paper II**, the two-dimensional analysis of the particulate silica hydrogels showed a non-linear correlation between pore size and flow measurements. Since a large part of the pore connectivity is obscured in two dimensions, it was motivated to acquire the three-dimensional tomograms (presented here) for the further study of mass transport with a three-dimensional approach performed in **Paper V**.

6.5 Paper V

Using the reconstructed three-dimensional ET tomograms of the particulate silica hydrogels from **Paper IV**, we characterised the pore network in three dimensions in terms of pore size distribution, pore morphology (skeletonisation) and fractal dimension (D_f). The tomograms were used as templates for Lattice Boltzmann modelling of mass transport in the gels. The motivation for this paper was to elucidate links between the three-dimensional nanostructure of the particulate silica hydrogel pore network and its liquid transport properties, using three-dimensional structural data.

The analysis showed that the D_f of the different gels were in the range between 2.0 and 2.2. This corresponds well to previous studies where the data was collected in a similar way.

The geometrical evaluation of the pore size distribution for the mirrored samples showed that the tomogram for Gel 1 had pores up to approximately 450 nm with the main part between 70 nm and 250 nm. For Gel 2 and 3, the histograms looked surprisingly similar, with a maximum detected pore size of 100-120 nm. However, a larger part of the pores of Gel 3 was concentrated to values between 20 nm and 50 nm, while the larger part of the Gel 2 pores was in a slightly wider range. One reason for this apparent similarity might be the loss of fine structure data during visualisation as a consequence of the missing wedge artefact.

From the skeletonisation of the pore structure, we could quantitatively compare the pore networks of the gels using the nearest-neighbour histogram of the skeleton, which enabled comparison between the hydrogel structures regardless of the length scale and magnification. The gels presented almost identical histograms, which strongly indicated that the pore network structures were very similar in terms of pore shape and tortuosity of their pore network.

As a final and important step, we evaluated the LBM output in the context of representative volume. From a simulated RLCA structure, we extracted slices of increasing thickness. These slices were then used for LBM, with either the mirrored or the periodic boundary condition (equivalent to the procedure for the LBM in the tomograms). The LBM results for the tomograms of the different gels could consequently be compared to the results for the simulated structures. In this plot, it is shown how the accuracy of the permeability simulations increases with sample thickness. The permeability results for mirrored and periodic boundary conditions are clearly converging towards a representative sample volume for LBM. We can also clearly see that Gel 2 is in the region of representative volume. Hence, we expected the simulated permeability values for Gel 2 to be the best corresponding to the experimental data. However, the differences between the simulated and measured permeabilities were large for all gels.

The paper demonstrated a methodology for research and development of materials with specific mass transport properties: three-dimensional imaging, three-dimensional pore network analysis and three-dimensional mass transport simulations. However, the challenges of sample thickness in relation to LBM still remains for the future.

This paper is the direct continuation of both **Paper II** and **Paper IV**. From **Paper II**, the need for *three-dimensional* analysis of the pore network with focus on mass transport properties was made clear. This data was provided in **Paper IV**, which also included analysis of the pore network connectivity properties.

Chapter 7

Summary of work

This work has focused towards the direct connection between the detailed and local nanostructure of particulate silica hydrogels and mass transport properties or aggregation dynamics. The combination of ET and advanced preparation techniques for high-resolution microscopy provides unique structure information for understanding structure-transport relationships. The porosity length scale of the three different PSH samples was selected to reflect a length scale where the exact influence of flow versus diffusion is experimentally unknown, and highly dependant on material structure. I used 2D and 3D imaging (STEM and ET) to characterise the different particulate silica hydrogels concerning the primary particle size and morphology, fractal dimension, pore size distribution, pore morphology, pore interconnectivity and accessible pore volume fraction. The data were compared to the mass transport data on both flow and diffusion. The STEM micrographs were also used for quantitative statistical modelling of the material structure in three dimensions, using the log-likelihood method, and statistical modelling of the aggregation dynamics mechanisms (DLCA or RLCA). Statistical summary functions were used for a quantitative comparison of the experimental and the simulated data. One unique aspect of the study is that the reconstructed 3D nanoscale structure has been used for *in situ* LBM mass transport simulations and compared with mass transport measurements.

7.1 Conclusions

For determining the local three-dimensional nanoscale structure, we have used ET. From the tomogram of the PSHs, the pore interconnectivity and accessible pore volume fraction were determined using image analysis. We also used STEM micrographs with the maximum likelihood approach, for forming a 3D image from a 2D micrograph. Both these approaches was useful for the aggregation dynamics studies. STEM was concluded to be superior to TEM, due to the resolution of the tomograms and the dynamic focus option..

ET enables the determination of the detailed structure of thin samples of particulate silica hydrogels in three dimensions. Two possibilities which open up from using ET for imaging PSHs is i) to perform LBM simulations of mass transport *in situ* in the actual nanoscale pore structure, and ii) to use the material structure as a blue-print to aggregation dynamics studies performed by computer simulations. This would not have been possible with other 3D imaging techniques such as FIB-SEM or APT, since they have their optimised resolution span on either a too large or too small length scale.

The limitation of the ET technique as applied in this work turned out to be the effective thickness during tilt series acquisition, as previously suggested[113]. The PSH samples have a limited thickness, which is a limitation which we addressed by stacking the tomograms, for interconnectivity and accessible pore volume measurements but also for the *in situ* LBM of mass transport.

Concerning the *in situ* LBM of mass transport and the interconnectivity and accessible pore

volume fraction, the 2D information is simply not enough to form any conclusions on a larger length scale. This has previously been confirmed[27, 28]. Our results in **Paper V** show that 3D data are needed for an accurate determination of the mean pore size and in order for the flow simulations to be realistic. However, sections as thin as five particle diameters provided a fair mean pore size. In order for the LBM to give reasonable values, we showed that much larger volumes were needed.

The mass transport in the three investigated gels was impacted by the pore size distribution of the gels. Our results from the two-dimensional pore size analysis experimentally verified the existence of a non-linear relationship between pore size and flow speed at the investigated length scales. The coarser gel was separated from the other two by a factor of 4.3 in flow speed. The two finer gels presented almost identical flow speed data, although, their stereologically measured pore sizes differed with a factor of 3.3 ± 1.1 . From this, we conclude that for gels having a VWMV less than approximately 120 nm, the water transport will be independent of pore size. From the PSD in 3D, this correlation is no longer as clear. The three-dimensional data showed that the difference in structure between the two finer gels are smaller than anticipated from the study in 2D. Here, further research is needed starting with a thicker tomogram of the finest gel, and attending to the possible loss of finer structures originating from the ET technique.

The RLCA model with the lowest aggregation probability that was possible to simulate ($p = 0.00001$), was the p which agreed best with the 2D and the 3D structure of the coarsest particulate silica hydrogel (Gel 1). This was the case when comparing to either microscopy data or tomography data. However, the 3D data provides a nearly perfect match to the simulated structure, in contrast to the comparison with 2D data, which starts to diverge already at one particle radius.

The difficulties of aggregation dynamics determination from 2D micrographs was addressed first by performing computer modelling of the aggregation dynamics for creating different particulate gel structures. The two-dimensional and three-dimensional experimental structures were then used as validation for the comparison of the different models and the experimental data. This was performed using a set of summary functions in spatial statistics. Already from the 2D data, it was possible to see that the lowest aggregation probability was the best match to the structure. However, our preliminary results with a 3D data comparison showed that this provided a better match than the 2D data.

7.2 Outlook

For future 3D investigations, it would be interesting to use rod like samples in order to avoid the MW artefact, due to increasing sample thickness[113]. However, this approach is not straight forward for soft materials and there are some obstacles to get past in order to have a working acquisition method for rod shaped or needle like samples. An alternative way to circumvent the MW artefact is to use an iterative reconstruction technique based on prior knowledge. In our case, an algorithm addressing porous samples would be especially beneficial[76]. Another approach useful for reducing the artefacts of the tomograms can be by the recently demonstrated semi-automatic machine-learning approach to segmentation[108].

In recent years, several algorithms where prior knowledge of the samples is used during the reconstruction process, have been presented. Examples of this are the compressed sensing algorithm (which applies to samples that can be sparsely represented)[44], the discrete tomography algorithm (where the number of gray levels reconstruction has to be properly estimated)[115] and the PORES algorithm (where the fact that the material is porous is known)[76]. A useful feature of all these algorithms is that the acquiring procedure of the tilt series does not have to be altered in any way in order to use them. One or several of these new algorithms could prove useful for this work in the near future.

Simulating mass transport through the reconstructed structure provides an important step towards understanding mass transport in porous nanoscale materials. Our initial intension was also to perform LBM of flow in tomograms of lower magnification. However, these tomograms

(**Paper IV**) were somewhat curved, which complicating the simulations. Hence, this is a future challenge to overcome. Also, a valuable complement to these simulations can be simulations in structures where the whole material structure has been produced by computer simulation, based on a cluster aggregation model which has been validated using three-dimensional experimental structural data of the PSH.

The information obtained by studying silica nanoparticle gels can also be useful concerning other soft porous materials where mass transport is important. For example, our results on when either diffusion or convective flow is the dominating liquid transport mechanism have recently showed to be relevant for research in diverse fields from basic diffusion science[120] to biotechnology[121].

Since PSHs are used within battery science[7], and as porous materials are used in a great diversity of applications, for example[1], pharmaceuticals[2], catalysts[3, 4], fuel cell science[5] and solar cells[9, 10], I think and hope that my research in the long run could contribute progress within the field of renewable energy, as well as in the field of functional foods and better and more individually adjusted controlled release from pharmaceuticals.

Acknowledgements

I take this opportunity to express my appreciation to several persons who contributed in various ways to this work and to the writing of this thesis.

I acknowledge my main supervisor and group leader Eva Olsson for providing support and guidance concerning the wider perspective, as well as the finer details of science and scientific communication. I would also like to thank my former main supervisor Anne-Marie Hermansson, and my co-supervisors Niklas Lorén and Stefan Gustafsson, and my mentor Annika Altskär for helping me with everything from research questions to technical writing. All your help has been extremely valuable to me.

Thank you Mikael Persson at AkzoNobel PPC AB, for all your help regarding the properties and applications of silica, for answering all my questions, for providing me with sample material and for taking interest in my work.

Matias Nordin, Christoffer Abrahamsson, Aila Särkkä, and Mats Rudemo: Thank you for great collaboration and scientific contributions, for answering all my questions about your individual areas of expertise, and for taking interest in my work. Tobias Gebäck, Henrike Häbel, I really appreciate your hard work and valuable contributions on the final two manuscripts!

I also acknowledge Dr. Hamed Heidari and Prof. Sara Bals in the Electron microscopy for materials science (EMAT) group at the University of Antwerp, and Dr. Zineb Saghi and Prof. Paul Midgley in the Electron microscopy group at the University of Cambridge: Thank you all for sharing your expertise and providing valuable input on both 3D imaging of nanomaterials, and their reconstruction.

A great thank you to Anders Kvist, Ola Löfgren and Katarina Logg in the Chalmers Materials Analysis Laboratory group, for your never-ending patience and help regarding the instruments and computers.

I thank all my past and present colleagues in the Eva Olsson group, the Materials Microstructure group and the former Microscopy and Microanalysis group at the Department of Applied Physics. Thank you also to all the past and present colleagues of the Structure and Materials Design department at SP Food and Bioscience. A special thanks to my officemates Ludvig de Knoop, Wolfgang Jäger and Markus Löffler for your words of encouragement, for raising my spirit, for starting up (Markus) and maintaining (Ludvig) my coffee drinking habits.

I thank the SuMo Biomaterials collaboration for providing a stimulating research environment, and I thank all my colleagues within the collaboration, both from academia and industry. I also express my gratitude to VINNOVA and the Swedish foundation for strategic research (SSF), for funding my research project, and the ESTEEM2 collaboration for providing connections within all of Europe.

A special thank you to Mattias Goksör, Caroline B. Adiels and Amin Banaeiyan in the Biophotonics group at Göteborg University. Thank you for still making me feel right at home in your group, and for your ever-lasting support, encouragement, friendship and *patience*. Thank you also to Martin Adiels, for the last-minute support on deciphering strange mathematics.

Thank you Anna-Karin Gustavsson and Edit Helgee for support and nice tea-breaks from time to time, and thank you all of my friends whom I don't have enough room to mention by name!

Thank you to my parents Annette and Per Hamngren for encouraging me to keep studying, and to my brother Daniel Hamngren and Louise Linné for inspiration about life!

Thank you Valter for being the smartest and most adorable child. I have been longing to spending more time with you again, and now I finally can!

Last but not least, I pay very special appreciations to my husband Peter Blomqvist, without whom's endless support and patience I could never have finished the thesis work. Thank you for always encouraging me, even when I am stressed out and self-conscious.

Göteborg, 15th December 2016
Charlotte Hamngren Blomqvist

Bibliography

- [1] A.-M. HERMANSSON, N. LORÉN, AND M. NYDÉN, The importance of microstructure for solvent and solute diffusion on the micro and nano length scales, In P. Buera, J. Welti-Chanes, P. Lillford, and H. Corti, editors, *Water properties of Food, Pharmaceuticals and Biological Materials*, CRC Taylor and Francis, Boca Raton, FL (2006).
- [2] Y. QUI AND G. F. ZHANG, Research and Development Aspects of Oral Controlled-Release Dosage Forms, In D. L. Wise, editor, *Handbook of Pharmaceutical Controlled Release Technology*, Marcel Dekker Inc. (2000).
- [3] E. P. W. WARD, T. J. V. YATES, J. J. FERNANDEZ, D. E. W. VAUGHAN, AND P. A. MIDGLEY, Three-dimensional nanoparticle distribution and local curvature of heterogeneous catalysts revealed by electron tomography, *Journal of Physical Chemistry C* **111**, 11501–11505 (2007).
- [4] F. ZAERA, Nanostructured materials for applications in heterogeneous catalysis, *Chemical Society Reviews* **42**, 2746–2762 (2013).
- [5] M. L. ANDERSON, R. M. STROUD, AND D. R. ROLISON, Enhancing the activity of fuel-cell reactions by designing three-dimensional nanostructured architectures: Catalyst-modified carbon-silica composite aerogels, *Nano Letters* **2**, 235–240 (2002).
- [6] G. AKZONOBEL CHEMICALS, Bindzil GB Colloidal Silica Dispersion For the Lead-Acid Battery Industry (2011).
- [7] D. W. H. LAMBERT, P. H. J. GREENWOOD, AND M. C. REED, Advances in gelled-electrolyte technology for valve-regulated lead-acid batteries, *Journal of power sources* **107**, 173–179 (2002).
- [8] J. NORDSTRÖM, A. MATIC, J. Z. SUN, M. FORSYTH, AND D. R. MACFARLANE, Aggregation, ageing and transport properties of surface modified fumed silica dispersions, *Soft Matter* **6**, 2293–2299 (2010).
- [9] O. BÄCKE, C. LINDQVIST, A. D. D. MENDEZA, S. GUSTAFSSON, E. G. WANG, M. R. ANDERSSON, C. MÜLLER, AND E. OLSSON, Mapping fullerene crystallization in a photovoltaic blend: an electron tomography study, *Nanoscale* **7**, 8451–8456 (2015).
- [10] Y. J. SUH, N. LU, S. Y. PARK, T. H. LEE, S. H. LEE, D. K. CHA, M. G. LEE, J. HUANG, S. S. KIM, B. H. SOHN, G. H. KIM, M. J. KO, J. KIM, AND M. J. KIM, Three-dimensional observation of TiO₂ nanostructures by electron tomography, *Micron* **46**, 35–42 (2013).
- [11] C. ABRAHAMSSON, L. NORDSTIERNA, J. BERGENHOLTZ, A. ALTSKÄR, AND M. NYDÉN, Magnetically induced structural anisotropy in binary colloidal gels and its effect on diffusion and pressure driven permeability, *Soft Matter* **10**, 4403 – 4412 (2014).

- [12] E. SCHUSTER, J. ECKARDT, A.-M. HERMANSSON, A. LARSSON, N. LORÉN, A. ALTSKÄR, AND A. STRÖM, Microstructural, mechanical and mass transport properties of isotropic and capillary alginate gels, *Soft Matter* **10**, 357–366 (2014).
- [13] S. WASSÉN, R. BORDES, T. GEBÄCK, D. BERNIN, E. SCHUSTER, N. LORÉN, AND A.-M. HERMANSSON, Probe diffusion in phase-separated bicontinuous biopolymer gels, *Soft Matter* **10**, 8276–8287 (2014).
- [14] ROYAL SOCIETY OF CHEMISTRY. About Soft Matter. <http://www.rsc.org/publishing/journals/sm/about.asp>. Accessed March 30, 2014.
- [15] A.-M. HERMANSSON, Water- and Fatholding, In J. R. Mitchell and D. A. Ledward, editors, *Functional properties of food macromolecules*, pages 273–314, Elsevier Inc., Waltham, MA (1986).
- [16] J. C. ASHWORTH, S. M. BEST, AND R. E. CAMERON, Quantitative architectural description of tissue engineering scaffolds, *Materials Technology* **29**, 281–295 (2014).
- [17] J. C. ASHWORTH, M. MEHR, P. G. BUXTON, S. M. BEST, AND R. E. CAMERON, Cell Invasion in Collagen Scaffold Architectures Characterized by Percolation Theory, *Advanced Healthcare Materials* **4**, 1317–1321 (2015).
- [18] L. E. BECKINGHAM, C. A. PETERS, W. UM, K. W. JONES, AND W. B. LINDQUIST, 2D and 3D imaging resolution trade-offs in quantifying pore throats for prediction of permeability, *Advances in Water Resources* **62**, 1–12 (2013).
- [19] K. A. HING, S. M. BEST, K. E. TANNER, W. BONFIELD, AND P. A. REVELL, Mediation of bone ingrowth in porous hydroxyapatite bone graft substitutes, *Journal of Biomedical Materials Research Part A* **68A**, 187–200 (2004).
- [20] M. RÖDING, E. SCHUSTER, K. LOGG, M. LUNDMAN, P. BERGSTRÖM, C. HANSON, T. GEBÄCK, AND N. LORÉN, Computational high-throughput screening of fluid permeability in heterogeneous fiber materials, *Soft Matter* **12**, 6293–6299 (2016).
- [21] B. TJADEN, J. LANE, P. J. WITHERS, R. S. BRADLEY, D. J. L. BRETT, AND P. R. SHEARING, The application of 3D imaging techniques, simulation and diffusion experiments to explore transport properties in porous oxygen transport membrane support materials, *Solid State Ionics* **288**, 315–321 (2016).
- [22] B. WALTHER, N. LORÉN, M. NYDÉN, AND A.-M. HERMANSSON, Influence of kappa-carrageenan gel structures on the diffusion of probe molecules determined by transmission electron microscopy and NMR diffusometry, *Langmuir* **22**, 8221–8228 (2006).
- [23] A.-M. HERMANSSON, Gel characteristics - compression and penetration of blood-plasma gels, *Journal of Food Science* **47**, 1960–1964 (1982).
- [24] A.-M. HERMANSSON, Gel characteristics - structure as related to texture and waterbinding of blood-plasma gels, *Journal of Food Science* **47**, 1965–1972 (1982).
- [25] P. NELSON, *Biological physics - Energy, Information, Life*, W. H. Freeman and Company, New York, NY, USA, updated first edition (2008).
- [26] K. SOTT, T. GEBÄCK, M. PIHL, N. LORÉN, A. M. HERMANSSON, A. HEINTZ, AND A. RASMUSON, Micro-PIV methodology using model systems for flow studies in heterogeneous biopolymer gel microstructures, *Journal of Colloid and Interface Science* **398**, 262–269 (2013).

- [27] S. E. SILLIMAN, The importance of the third dimension on transport through saturated porous media: Case study based on transport of particles, *Journal of Hydrology* **179**, 181–195 (1996).
- [28] N. LORÉN, H. HAGSLÄTT, M. NYDÉN, AND A.-M. HERMANSSON, Water mobility in heterogeneous emulsions determined by a new combination of confocal laser scanning microscopy, image analysis, nuclear magnetic resonance diffusometry, and finite element method simulation, *Journal of Chemical Physics* **122** (2005).
- [29] F. L. ZHAO, D. YAO, R. W. GUO, L. D. DENG, A. J. DONG, AND J. H. ZHANG, Composites of Polymer Hydrogels and Nanoparticulate Systems for Biomedical and Pharmaceutical Applications, *Nanomaterials* **5**, 2054–2130 (2015).
- [30] T. SUGAR AND F. CUBA, An Electron Microscope Study of the Structure of Silica Gels, In R. Ross, editor, *Proc. of the Third International Conference on Electron Microscopy, London 1954*, pages 530–532, Royal Microscopical Society (1956).
- [31] R. A. L. JONES, *Soft Condensed Matter*, Oxford University Press Inc., New York, NY, USA (2002).
- [32] J. ROUQUEROL, D. AVNIR, C. W. FAIRBRIDGE, D. H. EVERETT, J. H. HAYNES, N. PERNICONE, J. D. F. RAMSAY, K. S. W. SING, AND K. K. UNGER, Recommendations for the characterization of porous solids, *Pure and Applied Chemistry* **66**, 1739–1758 (1994).
- [33] P. A. C. GANE, C. J. RIDGWAY, E. LEHTINEN, R. VALIULLIN, I. FURO, J. SCHOELKOPF, H. PAULAPURO, AND J. DAICIC, Comparison of NMR cryoporometry, mercury intrusion porosimetry, and DSC thermoporometry in characterizing pore size distributions of compressed finely ground calcium carbonate structures, *Industrial & Engineering Chemistry Research* **43**, 7920–7927 (2004).
- [34] A. GUEVEN AND Z. HICSASMAZ, *Pore Structure in Food: Simulation, Measurement and Applications*, volume VIII, Springer, cop., New York, USA; London, UK (2013).
- [35] S. JAGANATHAN, H. V. TAFRESHI, AND B. PPURDEYHIMI, Modeling liquid porosimetry in modeled and imaged 3-D fibrous microstructures, *Journal of Colloid and Interface Science* **326**, 166–175 (2008).
- [36] M. THOMMES AND K. A. CYCHOSZ, Physical adsorption characterization of nanoporous materials: progress and challenges, *Adsorption-Journal of the International Adsorption Society* **20**, 233–250 (2014).
- [37] R. SCHMIDT, E. W. HANSEN, M. STOECKER, D. AKPORIAYE, AND O. H. ELLESTAD, Pore-size determination of MCM-41 mesoporous materials by means of H-1-NMR spectroscopy, N-2 adsorption, and HREM - a preliminary-study, *Journal of the American Chemical Society* **117**, 4049–4056 (1995).
- [38] K. ISHIKIRIYAMA, M. TODOKI, AND K. MOTOMURA, Pore-size distribution (PSD) measurements of silica-gels by means of differential scanning calorimetry .1. Optimization for determination of PSD, *Journal of Colloid and Interface Science* **171**, 92–102 (1995).
- [39] K. ISHIKIRIYAMA AND M. TODOKI, Pore-size distribution (PSD) measurements of silica-gels by means of differential scanning calorimetry .2. Thermoporometry, *Journal of Colloid and Interface Science* **171**, 103–111 (1995).
- [40] J. J. HOWARD AND W. E. KENYON, Determination of pore-size distribution in sedimentary-rocks by proton nuclear-magnetic-resonance, *Marine and Petroleum Geology* **9**, 139–145 (1992).

- [41] S. LOWELL, J. SHIELDS, M. THOMAS, AND M. THOMMES, *Characterization of Porous Solids and Powders: Surface Area, Pore Size and Density*, volume 16, Kluwer Academic Publishers, Dordrecht, The Netherlands (2004).
- [42] P. A. MIDGLEY, M. WEYLAND, J. M. THOMAS, AND B. F. G. JOHNSON, Z-Contrast tomography: a technique in three-dimensional nanostructural analysis based on Rutherford scattering, *Chemical communications* pages 907–908 (2001).
- [43] P. ERCIUS AND D. MULLER, Incoherent Bright Field STEM for Imaging and Tomography of Ultra-Thick TEM Cross-sections, *Microscopy and Microanalysis* **15**, 238–239 (2009).
- [44] Z. SAGHI, D. J. HOLLAND, R. LEARY, A. FALQUI, G. BERTONI, A. J. SEDERMAN, L. F. GLADDEN, AND P. A. MIDGLEY, Three-Dimensional Morphology of Iron Oxide Nanoparticles with Reactive Concave Surfaces. A Compressed Sensing-Electron Tomography (CS-ET) Approach, *Nano letters* **11**, 4666–4673 (2011).
- [45] P. ALBERS, M. MAIER, M. REISINGER, B. HANNEBAUER, AND R. WEINAND, Physical boundaries within aggregates - differences between amorphous, para-crystalline, and crystalline Structures, *Crystal Research and Technology* **50**, 846–865 (2015).
- [46] T. ALTANTZIS, B. GORIS, A. SANCHEZ-IGLESIAS, M. GRZELCZAK, L. M. LIZ-MARZAN, AND S. BALS, Quantitative Structure Determination of Large Three-Dimensional Nanoparticle Assemblies, *Particle & Particle Systems Characterization* **30**, 84–88 (2013).
- [47] F. DALMAS, N. GENEVAZ, M. ROTH, J. JESTIN, AND E. LEROY, 3D Dispersion of Spherical Silica Nanoparticles in Polymer Nanocomposites: A Quantitative Study by Electron Tomography, *Macromolecules* **47**, 2044–2051 (2014).
- [48] A. DAS, R. BOLDT, R. JURK, D. JEHNICHEN, D. FISCHER, K. W. STOCKELHUBER, AND G. HEINRICHAC, Nano-scale morphological analysis of graphene-rubber composites using 3D transmission electron microscopy, *Rsc Advances* **4**, 9300–9307 (2014).
- [49] S. KOHJIYA, A. KATO, AND Y. IKEDA, Visualization of nanostructure of soft matter by 3D-TEM: Nanoparticles in a natural rubber matrix, *Progress in Polymer Science* **33**, 979–997 (2008).
- [50] D. AVNIR, T. CORADIN, O. LEV, AND J. LIVAGE, Recent bio-applications of sol-gel materials, *Journal of Materials Chemistry* **16**, 1013–1030 (2006).
- [51] R. K. ILER, *The Chemistry of Silica - Solubility, Polymerization, Colloid and Surface Properties, and Biochemistry*, John Wiley and Sons, Inc., Hoboken, NJ, USA (1979).
- [52] H. WU, J.-J. XIE, AND M. MORBIDELLI, Kinetics of colloidal gelation and scaling of the gelation point, *Soft Matter* **9**, 4437–4443 (2013).
- [53] AKZONOBEL PPC AB. Ground Consolidation: Building with stability. https://www.akzonobel.com/colloidalsilica/application/ground_consolidation/index.aspx. Accessed March 27, 2014.
- [54] M. R. NOLL, C. BARTLETT, AND T. M. DOCHAT, In Situ permeability reduction and chemical fixation using colloidal silica, In *Sixth National Outdoor Action Conference on Aquifer Restoration, sponsored by National Ground Water Assn.*, Las Vegas, NV (1992).
- [55] X. J. CAO, H. Z. CUMMINS, AND J. F. MORRIS, Structural and rheological evolution of silica nanoparticle gels, *Soft Matter* **6**, 5425–5433 (2010).

- [56] A. SCHANTZ ZACKRISSON, J. S. PEDERSEN, AND J. BERGENHOLTZ, A small-angle X-ray scattering study of aggregation and gelation of colloidal silica, *Colloids and surfaces A - physicochemical and engineering aspects* **315**, 23–30 (2008).
- [57] T. R. HOARE AND D. S. KOHANE, Hydrogels in drug delivery: Progress and challenges, *Polymer* **49**, 1993–2007 (2008).
- [58] H. ZOU, S. S. WU, AND J. SHEN, Polymer/silica nanocomposites: Preparation, characterization, properties, and applications, *Chemical Reviews* **108**, 3893–3957 (2008).
- [59] N. NASSIF, O. BOUVET, M. N. RAGER, C. ROUX, T. CORADIN, AND J. LIVAGE, Living bacteria in silica gels, *Nature Materials* **1**, 42–44 (2002).
- [60] A. SCHANTZ ZACKRISSON, A. MARTINELLI, A. MATIC, AND J. BERGENHOLTZ, Concentration effects on irreversible colloid cluster aggregation and gelation of silica dispersions, *Journal of colloid and interface science* **301**, 137–144 (2006).
- [61] G. W. SEARS, DETERMINATION OF SPECIFIC SURFACE AREA OF COLLOIDAL SILICA BY TITRATION WITH SODIUM HYDROXIDE, *Analytical Chemistry* **28**, 1981–1983 (1956).
- [62] M. PERSSON. Private communication (2014). AkzoNobel, PPC AB.
- [63] D. B. WILLIAMS AND B. C. CARTER, *Transmission electron microscopy : a textbook for materials science*, Springer, cop., New York, USA; London, UK, 2nd edition (2009).
- [64] P. BLEUET, G. AUDOIT, J.-P. BARNES, J. BERTHEAU, Y. DABIN, H. DANSAS, J.-M. FABRI, B. FLORIN, P. GERGAUD, A. GRENIER, G. HABERFEHLNER, E. LAY, J. LAURENCIN, R. SERRA, AND J. VILLANOVA, Specifications for Hard Condensed Matter Specimens for Three-Dimensional High-Resolution Tomographies, *Microscopy and microanalysis* **19**, 726–739 (2013).
- [65] J. FRANK, *Electron Tomography: Methods for Three-Dimensional Visualization of Structures in the Cell*, Springer (2006).
- [66] A. J. KOSTER, H. CHEN, J. W. SEDAT, AND D. A. AGARD, Automated microscopy and microscopy for electron tomography, *Ultramicroscopy* **46**, 207–227 (1992).
- [67] P. A. MIDGLEY AND M. WEYLAND, 3D electron microscopy in the physical sciences: the development of Z-contrast and EFTEM tomography, *Ultramicroscopy* **96**, 413–431 (2003).
- [68] P. W. HAWKES, The electron microscope as a structure projector, In J. Frank, editor, *Electron Tomography: Methods for Three-Dimensional Visualization of Structures in the Cell*, pages 83–112, Springer (2006).
- [69] M. WEYLAND AND P. MIDGLEY, Electron Tomography, In D. Williams and C. Carter, editors, *Transmission Electron Microscopy*, pages 343–376, Springer International Publishing (2016).
- [70] A. KLUG AND J. T. FINCH, Structure of viruses of papilloma-polyoma type .I. Human wart virus, *Journal of molecular biology* **11**, 403–423 (1965).
- [71] W. O. SAXTON, W. BAUMEISTER, AND M. HAHN, 3-dimensional reconstruction of imperfect two-dimensional crystals, *Ultramicroscopy* **13**, 57–70 (1984).
- [72] J. RADON, On the determination of functions from their integrals along certain manifolds, *Berichte uber die Verhandlungen der Koniglich Sachsische Gesellschaft der Wissenschaften zu Leipzig, Mathematisch-Physikalische (translated)* **69**, 262–277 (1917).

- [73] P. ERCIUS, M. WEYLAND, D. A. MULLER, AND L. M. GIGNAC, Three-dimensional imaging of nanovoids in copper interconnects using incoherent bright field tomography, *Applied Physics Letters* **88** (2006).
- [74] M. NIEHLE AND A. TRAMPERT, Electron tomography on nanopores embedded in epitaxial GaSb thin films, *Micron* **73**, 54–62 (2015).
- [75] D. STOECKEL, C. KÜBEL, K. HORMANN, A. HÖLTZEL, B. M. SMARSLY, AND U. TALLAREK, Morphological Analysis of Disordered Macroporous-Mesoporous Solids Based on Physical Reconstruction by Nanoscale Tomography, *Langmuir* **30**, 9022–9027 (2014).
- [76] G. VAN EYNDHOVEN, M. KURTTEPELI, C. J. VAN OERS, P. COOL, S. BALS, K. J. BATENBURG, AND J. SIJBERS, Pore REconstruction and Segmentation (PORES) method for improved porosity quantification of nanoporous materials, *Ultramicroscopy* **148**, 10–19 (2015).
- [77] A. L. PARRY, P. H. H. BOMANS, S. J. HOLDER, N. SOMMERDIJK, AND S. C. G. BIAGINI, Cryo Electron Tomography Reveals Confined Complex Morphologies of Tripeptide-Containing Amphiphilic Double-Comb Diblock Copolymers, *Angewandte Chemie-International Edition* **47**, 8859–8862 (2008).
- [78] B. V. ANDERSSON, A. HERLAND, S. MASICH, AND O. INGANS, Imaging of the 3D nanostructure of a polymer solar cell by electron tomography, *Nano Letters* **9**, 853–855 (2009).
- [79] P. K. LUTHER, Sample shrinkage and radiation damage of plastic sections, In J. Frank, editor, *Electron Tomography: Methods for Three-Dimensional Visualization of Structures in the Cell*, pages 17–48, Springer (2006).
- [80] H. HEIDARI, W. VAN DEN BROEK, AND S. BALS, Quantitative electron tomography: The effect of the three-dimensional point spread function, *Ultramicroscopy* **135**, 1–5 (2013).
- [81] Y. CHENG, R. PRUD'HOMME, AND J. THOMAS, Diffusion of mesoscopic probes in aqueous polymer solutions measured by fluorescence recovery after photobleaching, *MACROMOLECULES* **35**, 8111–8121 (2002).
- [82] D. J. BEEBE, G. A. MENSING, AND G. M. WALKER, Physics and applications of microfluidics in biology, *Annual Review of Biomedical Engineering* **4**, 261–286 (2002).
- [83] C. SHU AND Z. GUO, *Lattice Boltzmann Method and Its Application in Engineering*, World Scientific Publishing Company (2013).
- [84] L. MASARO AND X. X. ZHU, Physical models of diffusion for polymer solutions, gels and solids, *Progress in polymer science* **24**, 731–775 (1999).
- [85] S. BABU, J. C. GIMEL, AND T. NICOLAI, Tracer diffusion in colloidal gels, *Journal of Physical Chemistry B* **112**, 743–748 (2008).
- [86] H. J. M. VAN DIJK AND P. WALSTRA, Syneresis of Curd .2. One-dimensional Syneresis of Rennet Curd in Constant Conditions, *Netherlands Milk and Dairy Journal* **40**, 3–30 (1986).
- [87] F. TAVENAS, P. JEAN, P. LEBLOND, AND S. LEROUEIL, The permeability of natural soft clays .2. Permeability characteristics, *Canadian Geotechnical Journal* **20**, 645–660 (1983).
- [88] M. MELLEMA, J. W. M. HEESAKKERS, J. H. J. VAN OPHEUSDEN, AND T. VAN VLIET, Structure and scaling behavior of aging rennet-induced casein gels examined by confocal microscopy and permeametry, *Langmuir* **16**, 6847–6854 (2000).

- [89] W. S. PRICE, *Pulsed-Field Gradient Nuclear Magnetic Resonance as a Tool for Studying Translational Diffusion: Part 1. Basic Theory*, John Wiley & Sons, Inc., Hoboken, NJ (1997).
- [90] P. GREENWOOD, H. LAGNEMO, AND M. REED. Composition prepared from silica sol and mineral acid Mar. 9 2010. US Patent 7,674,833.
- [91] G. MIE, Beiträge zur Optik trüber Medien, speziell kolloidaler Metallösungen, *Annalen der Physik* **330**, 377–445 (1908).
- [92] H. B. WEN, J. MORADIAN-OLDAK, W. LEUNG, P. BRINGAS, AND A. G. FINCHAM, Microstructures of an amelogenin gel matrix, *Journal of Structural Biology* **126**, 42–51 (1999).
- [93] J. AYACHE, *Sample preparation handbook for transmission electron microscopy: methodology*, Springer, cop., New York, USA; London, UK, 1st edition (2010).
- [94] A. R. SPURR, A low-viscosity epoxy resin embedding medium for electron microscopy, *Journal of ultrastructure research* **26**, 31–43 (1969).
- [95] A. CAVALIER, D. SPEHNER, AND B. M. HUMBEL, *Handbook of Cryo-Preparation Methods for Electron Microscopy*, CRC Press, Boca Raton, FL, USA (2009).
- [96] J. R. KREMER, D. MASTRONARDE, AND J. MCINTOSH, Computer visualization of three-dimensional image data using IMOD, *Journal of Structural Biology* **116**, 71–76 (1996).
- [97] J. C. RUSS, *Image analysis of food microstructure*, CRC Press LLC, Boca Raton, FL, USA (2005).
- [98] V. BRUSASCO AND A. T. DINH-XUAN, Stereology: a bridge to a better understanding of lung structure and function, *European respiratory journal* **35**, 477–478 (2010).
- [99] H. GUNDERSEN, T. BENDTSEN, L. KORBO, N. MARCUSSEN, A. MOLLER, K. NIELSEN, J. NYENGAARD, B. PAKKENBERG, F. SØRENSEN, A. VESTERBY, AND M. WEST, Some New, Simple and Efficient Stereological Methods and their Use in Pathological Research and Diagnosis - Review Article, *APMIS* **96**, 379–394 (1988).
- [100] H. J. G. GUNDERSEN, P. BAGGER, T. F. BENDTSEN, S. M. EVANS, L. KORBO, N. MARCUSSEN, A. MØLLER, K. NIELSEN, J. R. NYENGAARD, B. PAKKENBERG, F. B. SØRENSEN, A. VESTERBY, AND M. J. WEST, The New Stereological Tools - Disector, Fractionator, Nucleator and Point Sampled Intercepts and their Use in Pathological Research and Diagnosis, *APMIS* **96**, 857–881 (1988).
- [101] N. LORÉN, M. LANGTON, AND A.-M. HERMANSSON, Confocal Laser Scanning Microscopy and Image Analysis of Kinetically Trapped Phase-Separated Gelatin/Maltodextrin Gels, *Food Hydrocolloids* **13**, 185–198 (1999).
- [102] P. MOUTON, *Principles and Practices of Unbiased Stereology - An Introduction for Bioscientists*, The John Hopkins University Press, Baltimore, MA, USA (2002).
- [103] H. J. G. GUNDERSEN AND E. B. JENSEN, Stereological Estimation of the Volume-Weighted Mean Volume of Arbitrary Particles Observed on Random Sections, *Journal of Microscopy-Oxford* **138**, 127–142 (1985).
- [104] H. HÄBEL. Private communication (March, 2015). Chalmers University of Technology and University of Gothenburg, Department of Mathematical Sciences.
- [105] P. M. DIXON, Ripley's K function, In A. H. El-Shaarawi and W. W. Piegorsch, editors, *Encyclopedia of Environmetrics*, volume 3, pages 1796 – 1803, John Wiley & Sons, Ltd (2002).

- [106] S. S. BRANDT, Markerless alignment in electron tomography, In J. Frank, editor, *Electron Tomography: Methods for Three-Dimensional Visualization of Structures in the Cell*, pages 187–215, Springer (2006).
- [107] P. GILBERT, Iterative methods for 3-dimensional reconstruction of an object from projections, *Journal of theoretical biology* **36**, 105–117 (1972).
- [108] L. STANIEWICZ AND P. MIDGLEY, Machine learning as a tool for classifying electron tomographic reconstructions, *Advanced Structural and Chemical Imaging* **1**, 1–15 (2015).
- [109] M. J. MOORE, E. JABBARI, E. L. RITMAN, L. C. LU, B. L. CURRIER, A. J. WINDEBANK, AND M. J. YASZEMSKI, Quantitative analysis of interconnectivity of porous biodegradable scaffolds with micro-computed tomography, *Journal of Biomedical Materials Research Part A* **71A**, 258–267 (2004).
- [110] F. TARIQ, P. D. LEE, R. HASWELL, AND D. W. MCCOMB, The influence of nanoscale microstructural variations on the pellet scale flow properties of hierarchical porous catalytic structures using multiscale 3D imaging, *CHEMICAL ENGINEERING SCIENCE* **66**, 5804–5812 (2011).
- [111] H. HÄBEL, A. SÄRKKÄ, M. RUDEMO, C. HAMNGREN BLOMQVIST, E. OLSSON, C. ABRAHAMSSON, AND M. NORDIN, From static micrographs to particle aggregation dynamics in three dimensions, *Journal of Microscopy* **262**, 102–111 (2016).
- [112] D. CHEN, H. FRIEDRICH, AND G. DE WITH, On Resolution in Electron Tomography of Beam Sensitive Materials, *Physical Chemistry C* **118**, 1248–1257 (2014).
- [113] N. KAWASE, M. KATO, H. NISHIOKA, AND H. JINNAI, Transmission electron microtomography without the "missing wedge" for quantitative structural analysis, *Ultramicroscopy* **107**, 8–15 JAN 2007.
- [114] I. ARSLAN, J. R. TONG, AND P. A. MIDGLEY, Reducing the missing wedge: High-resolution dual axis tomography of inorganic materials, *Ultramicroscopy* **106**, 994–1000 (2006).
- [115] K. J. BATENBURG, S. BALS, J. SIJBERS, C. KUBEL, P. A. MIDGLEY, J. C. HERNANDEZ, U. KAISER, E. R. ENCINA, E. A. CORONADO, AND G. VAN TENDELOO, 3D imaging of nanomaterials by discrete tomography, *Ultramicroscopy* **109**, 730–740 (2009).
- [116] D. L. CHEN, B. GORIS, F. BLEICHRODT, H. H. MEZERJI, S. BALS, K. J. BATENBURG, G. DE WITH, AND H. FRIEDRICH, The properties of SIRT, TVM, and DART for 3D imaging of tubular domains in nanocomposite thin-films and sections, *Ultramicroscopy* **147**, 137–148 (2014).
- [117] J. C. RUSS AND R. T. DEHOFF, *Practical stereology*, Kluwer Academic, New York, NY, USA, 2nd edition (2000).
- [118] T. NISHIYAMA, K. KANEKO, K. YAMADA, R. TERANISHI, T. KATO, T. HIRAYAMA, T. IZUMI, AND Y. SHIOHARA, Microstructural characterization of TFA-MOD processed $Y_{1-x}Gd_xBa_2Cu_3O_{7-y}$ with $BaZrO_3$, *Micron* **5253**, 1 – 7 (2013).
- [119] E. KIRKLAND, *Advanced Computing in Electron Microscopy*, Springer, New York (1998).
- [120] A. ZHOKH, A. TRYPOLSKYI, AND P. STRIZHAK, An investigation of anomalous time-fractional diffusion of isopropyl alcohol in mesoporous silica, *International Journal of Heat and Mass Transfer* **104**, 493–502 (2017).
- [121] L. E. MARSHALL, R. KOOMULLIL, A. R. FROST, AND J. L. BERRY, Computational and Experimental Analysis of Fluid Transport Through Three-Dimensional CollagenMatrigel Hydrogels, *Annals of Biomedical Engineering* (2016).